Washington University in St. Louis
Washington University Open Scholarship

All Theses and Dissertations (ETDs)

5-24-2011

Ultrasound-encoded optical tomography and time-reversed ultrasonically encoded optical focusing

Xiao Xu
Washington University in St. Louis

Follow this and additional works at: https://openscholarship.wustl.edu/etd

Recommended Citation

Xu, Xiao, "Ultrasound-encoded optical tomography and time-reversed ultrasonically encoded optical focusing" (2011). *All Theses and Dissertations (ETDs)*. 876.
https://openscholarship.wustl.edu/etd/876

This Dissertation is brought to you for free and open access by Washington University Open Scholarship. It has been accepted for inclusion in All Theses and Dissertations (ETDs) by an authorized administrator of Washington University Open Scholarship. For more information, please contact digital@wumail.wustl.edu.

WASHINGTON UNIVERSITY IN ST. LOUIS
School of Engineering and Applied Science
Department of Biomedical Engineering

Dissertation Examination Committee:
Lihong V. Wang, Chair
Joseph Culver
Viktor Gruev
James Miller
Yoram Rudy
Jung-Tsung Shen

ULTRASOUND-ENCODED OPTICAL TOMOGRAPHY AND TIME-REVERSED ULTRASONICALLY ENCODED OPTICAL FOCUSING

by

Xiao Xu

A dissertation presented to the
Graduate School of Arts and Sciences
of Washington University in
partial fulfillment of the
requirements for the degree
of Doctor of Philosophy

August 2011
Saint Louis, Missouri

Copyright © by

Xiao Xu

2011

ABSTRACT OF THE DISSERTATION

Ultrasound-encoded Optical Tomography and Time-Reversed Ultrasonically Encoded Optical Focusing

by

Xiao Xu

Doctor of Philosophy in Biomedical Engineering

Washington University in St. Louis, 2011

Research Advisor: Professor Lihong V. Wang

Ultrasound modulated optical tomography is a developing hybrid imaging modality that combines high optical contrast and good ultrasonic resolution to image soft biological tissue. We developed a photorefractive crystal-based, time-resolved detection scheme with the use of a millisecond long ultrasound burst to image both the optical and mechanical properties of biological tissues, with improved detection efficiency of ultrasound-tagged photons.

We also applied spectral-hole burning (SHB) aided detection in ultrasound-modulated optical tomography (UOT) to image optical heterogeneities in thick tissue-mimicking phantom samples and chicken breast tissue. The efficiency of SHB was improved by using a Tm3+: YAG crystal of higher doping concentration (2.0-atomic%) and a double-pass pumping configuration. With the improved SHB-UOT system, we imaged absorbing, scattering, and phase contrast objects that were embedded in the middle plane of a 30-mm thick phantom sample. The imaging resolution was 0.5 mm in the lateral direction, as defined by the focal width of the ultrasonic transducer, and 1.5 mm in the axial direction, as determined by the ultrasonic burst length. We also imaged two absorbing objects embedded in the middle plane of a 32-mm thick chicken breast sample. The results suggest that the improved SHB-UOT system is one step closer to a practical optical imaging application in biological and clinical studies.

Light focusing plays a central role in biomedical imaging, manipulation, and therapy. In optical scattering media such as biological tissue, light propagation is randomized by multiple scattering. Beyond one transport mean free path, where photon propagation is in the diffusive regime, direct light focusing becomes infeasible. Although various methods have been developed to overcome this optical diffusion limit, all are limited by the lack of a practical internal "guide star." Here we proposed and experimentally validated a novel concept, called Time-Reversed Ultrasonically Encoded (TRUE) optical focusing, to deliver light dynamically into any predefined location inside a scattering medium. First, diffused coherent light is encoded by an ultrasonic wave focused to a predefined location; then, the encoded component of the diffused light is time-reversed and consequently converges back to the ultrasonic focus. The ultrasonic encoding noninvasively provides a virtual internal "guide star" for the time reversal. The TRUE optical focus—dynamically defined by the ultrasonic focus—is unaffected by multiple scattering of light, which is especially desirable in biological tissue where ultrasonic scattering is ~1000 times weaker than optical scattering. Various fields, such as biomedical, colloidal, atmospheric, and ocean optics, can benefit from TRUE optical focusing. Further, the concept can be generalized for non-optical waves.

Acknowledgments

I would like to express my sincere gratitude to my thesis advisor, Professor Lihong V. Wang, for his invaluable advice and support. His continuous guidance helped me stay focused in my research aims. I thank him for giving me an opportunity to work in an intellectually stimulating and friendly environment for research, for inspiring me with challenging ideas, and for helping me establish good working habits in research. Great thanks are also due for being available all the time to patiently correct my manuscripts. I would also like to thank him for teaching advanced biomedical optics with rigorous mathematical and computational approaches.

I thank my committee members, Dr. Joseph Culver, Dr. Viktor Gruev, Dr. James Miller, Dr. Yoram Rudy, and Dr. Jung-Tsung Shen for their constructive suggestions and time given to serve on my thesis committee.

I am grateful for the excellent courses and seminars during my graduate studies at Texas A&M University in College Station and Washington University in St. Louis. My sincere gratitude extends to all my teachers who taught me not only the knowledge to understand the world, but a curious mind to ask question, and to explore the unknown domain.

I am deeply indebted to my present and former collaborators, Huiliang Zhang, Kothapalli Sri-Rajasekhar, and Honglin Liu for their excellent work. The success of the research projects would not be possible without their great contributions.

I am thankful to Dr. Philip Hemmer at Texas A&M University in College Station, for his guidance through the photorefractive detection project and his help in revising the manuscript.

No words can express my deep sense of gratitude to my former colleague in the optical imaging laboratory, Dr. Geng Ku, for his hands-on help in the experiment and stimulating scientific discussion. Grateful thanks are also due to Dr. Konstatin Maslov for his timely help, technical assistance, and many scientific discussions.

I am grateful to my former and present colleagues, Jun Li, Sava Sakadzic, Dekui Qin, Shuliang Jiao, Jun Ai, Hao Zhang, Youzhi Li, Xinmai Yang, Changhui Li, Li Li, Puxiang Lai,

and all the other lab members, for all their support, technical assistance, scientific discussions, and friendship over these years, in and outside the lab.

Many thanks to the staff of the Biomedical Engineering departments at Texas A&M University in College Station, (Dr. Fidel Fernandez, Katherine Jakubik, and Barry Jackson), and Washington University in St. Louis (Shirley Eisenhauer, Amanda Moritz, Glen Reitz, and Karen Teasdale) for their help. A special thanks to Steve Smith at Texas A&M University for his help and patience during the long hours in the machine shop. Grateful thanks are also due to Jim Ballard and Sandra Matteucci at Washington University for editing all my manuscripts.

With great love, I thank my family for their love and unfailing support throughout my career.

Xiao Xu

Washington University in St. Louis
August 2011

Dedicated to my family

Contents

Abstract ii

Acknowledgments iv

List of Tables ix

List of Figures x

List of Abbreviations xii

1 Introduction 1
- 1.1 Ultrasound-modulated Optical Tomography (UOT) 1
  - 1.1.1 Biomedical Optical Imaging 1
  - 1.1.2 Diffuse Optical Imaging 4
  - 1.1.3 Ultrasound-modulated Optical Tomography 5
- 1.2 Signal Detection in UOT 5
  - 1.2.1 Photorefractive Detection for UOT 6
  - 1.2.2 Spectral-hole Burning Aided Detection for UOT 12
- 1.3 Time-Reversed Ultrasonically Encoded (TRUE) Optical Focusing 13

2 UOT with Photorefractive Detection 15
- 2.1 Optical Imaging and UOT 15
- 2.2 $Bi_{12}SiO_{20}$ (BSO) Photorefractive Crystal (PRC) 18
- 2.3 Experimental Methods 21
- 2.4 Results and Discussion 23
- 2.5 Conclusions 27

3 UOT with Spectral-hole Burning Detection 29
- 3.1 Spectral-hole Burning for UOT 29
- 3.2 Experimental Methods 30
  - 3.2.1 Tm^{3+}: YAG crystal used in SHB 30
  - 3.2.2 Experimental Set-up 31
- 3.3 Results and Discussion 33
- 3.4 Conclusions 41

4 Time-Reversed Ultrasonically Encoded Optical Focusing 43
- 4.1 Motivations 43
- 4.2 Working Principle and Experimental Implementation 44
  - 4.2.1 Working Principle and Experimental Set-up 44
  - 4.2.2 Monte Carlo Simulation 46

4.2.3 Experimental Validation 47
4.2.4 Comparison of TRUE Signal to Ballistic Light 50
4.3 Improving Optical Thickness in TRUE Focusing 52
4.3.1 Improved Experimental Set-up 53
4.3.2 Imaging Results 56
4.4 Discussion 61

5 Conclusions 63
5.1 Summary of Work Done 63
5.2 Directions for Future Work 65

Appendix A Two Dimensional Monte Carlo Simulation of Light Propagation inside a Scattering Slab 67

Appendix B Derivation of the Image Resolution in TRUE Optical Imaging Experiment 76

References 78

Vita 89

List of Tables

Table 2.1: Different signal detection methods in UOT ... 17
Table 2.2: Material parameters for BaTiO3, BSO, and GaAs ... 19
Table 2.3: Physical parameters of BSO at three wavelengths ... 20

List of Figures

Figure 1.1: Absorption spectra of several tissue types 3

Figure 1.2: Photorefractive effect 9

Figure 2.1: $Bi_{12}SiO_{20}$ Photorefractive crystal 21

Figure 2.2: Schematic of PRC-UOT experimental setup 22

Figure 2.3: UOT signal increase with increasing ultrasound burst length 24

Figure 2.4: UOT image of sample #2 25

Figure 2.5: UOT image (surface map) of sample #3 at T = 0.1 ms and 1.1 ms after the onset of a 1-ms long ultrasound burst. 26

Figure 2.6: Time resolved UOT image of sample #4 26

Figure 3.1: Energy transition in Tm^{3+}:YAG at $\lambda = 793.38$ nm 31

Figure 3.2: Schematic of SHB-UOT experimental setup 32

Figure 3.3: Comparison of the transmitted probe beam powers 33

Figure 3.4: UOT images of the absorbing, scattering, and phase contrast objects embedded in the middle plane of a 30-mm thick Intralipid phantom slab 35

Figure 3.5: UOT images of a 32-mm thick chicken breast sample 37

Figure 3.6: UOT image of the three absorbing objects embedded in the middle plane of a 40-mm thick tissue-mimicking phantom 39

Figure 3.7: Acoustic pressure contribution by the fundamental and second harmonic frequencies of a 5 MHz focused transducer at its focus, and the detected SHB-UOT signals when a spectral-hole was burned at the fundamental or second harmonic frequency 40

Figure 3.8: Harmonic image of two absorbing objects embedded in a 20-mm thick phantom sample 41

Figure 4.1: Schematic of the experimental setup for TRUE optical focusing 45

Figure 4.2: 2D Monte Carlo simulation of light propagation inside a scattering slab 46

Figure 4.3: Results from four imaging experiments validating TRUE focusing 49

Figure 4.4: An example waveform of the detected TRUE signal 51

Figure 4.5: Comparison of the experimental TRUE optical signal and the computed ballistic light signal at different thicknesses L 52
Figure 4.6: Schematic of the improved experimental setup for TRUE focusing........ 53
Figure 4.7: TRUE images of a phantom with an optical thickness of 37.5 57
Figure 4.8: TRUE image of a phantom with an optical thickness of 50 59
Figure 4.9: TRUE image of a phantom with an optical thickness of 70 60

List of Abbreviations

2D:	Two dimensional
3D:	Three dimensional
AC:	Alternating current
ANSI:	American National Standards Institute
B-scan:	Cross-sectional scan
BSO:	$Bi_{12}SiO_{20}$
CCD:	Charge coupled device
CT:	Computed tomography
CW:	Continuous wave
DOT:	Diffuse optical tomography
FOV:	Field of view
FWHM:	Full width at half maxima
MRI:	Magnetic resonance imaging
NA:	Numerical aperture
NIR:	Near infrared
OCT:	Optical coherence tomography
OPC:	Optical phase conjugation
PA:	Photoacoustic
PAT:	Photoacoustic tomography
PAM:	Photoacoustic microscopy
PCM:	Phase conjugate mirror
PET:	Positron emission tomography
PRC:	Photorefractive crystal
RF:	Radio frequency
SNR:	Signal-to-noise ratio
TR:	Time reversal or time-reversed
TRUE:	Time-reversed ultrasonically encoded (optical focusing)

UOT:	Ultrasound-encoded (or ultrasound-modulated) optical tomography

Chapter 1

Introduction

1.1 Ultrasound-modulated optical tomography

1.1.1 Biomedical Optical Imaging

The use of light to probe the structure of matter, e. g., biological tissues, is as old as the human eye. The invention of optical microscopy in the 1600s greatly enhanced human vision by magnifying images of small samples, and enabling the visualization of the fine structures and inner working of biological tissues on the cellular level. Despite the increasingly complex design of optical microscopes, the working principle for microscopic imaging has always been straightforward—the acquired image maps the optical properties of the sample; the image contrast is based on differential optical absorption, reflection, scattering, birefringence, etc.; and the sample is sectioned into thin slices so that light propagation through the sample can be modeled by simple geometric optics[1]. On the other hand, optical imaging methods that are not based on microscopy have also been explored as probes for biological structures. For example, the use of transillumination as a diagnostic aid in detecting breast lesions was reported as early as 1929[2], in which transillumination images or simple shadows of breast tumors were obtained by shining a flashlight through breast tissue. However, the lack of resolution due to the diffusive nature of light propagating through breast tissue makes it difficult to interpret the imaging results for reliable clinical diagnosis. It is for this reason that optical imaging did not gain popularity in biology and medicine until the late 1970s and 1980s, when a better understanding of the light and tissue interaction was being developed, and great technical advances, such as lasers and sensitive optical detectors, were being made. The application of optical imaging in biology and medicine, or biomedical optical imaging, is the subject of this dissertation. In particular, this study focuses on optical imaging of soft biological tissue.

Optical imaging of soft biological tissue is highly desirable in the biomedical field as a non-invasive, nonionizing, and functional imaging modality[3]. First of all, it is relatively inexpensive compared with magnetic resonance imaging (MRI). Second, it is safe for biological molecules because optical imaging typically uses low energy, nonionizing photons (e.g., ~2 eV for $\lambda = 500$ nm), as compared with the high energy, ionizing radiation used in X-ray imaging (e.g., ~50 KeV for X-ray photons). Third, it provides better soft-tissue contrast than the ultrasound imaging because its contrast is based on optical properties such as absorption and scattering of the tissue. Finally, optical imaging signals can serve as intrinsically sensitive indicators of tissue abnormalities and functions[4-6], because in the visible and near infrared wavelengths, the absorption and scattering properties of biological tissues are directly related to their molecular constituents and to the molecular, electronic, and/or vibrational structures.

Figure 1.1 illustrates the primary absorption spectra of several tissue types and tissue constituents, along with the absorption coefficients at some typical laser wavelengths[7]. Several things need to be pointed out: (1) For ultraviolet (UV) wavelengths, the primary absorbers in biological tissue are protein, DNA, and water. The absorption typically increases with decreasing wavelength. (2) In the infrared (IR) wavelength regime, water is the dominant absorber. (3) In the red to near-infrared (NIR) wavelengths, the absorption of biological tissues is the smallest, and the penetration of light is consequently the deepest. This region is ideally suited for biomedical applications, and thus is called the "diagnostic and therapeutic window"[8].

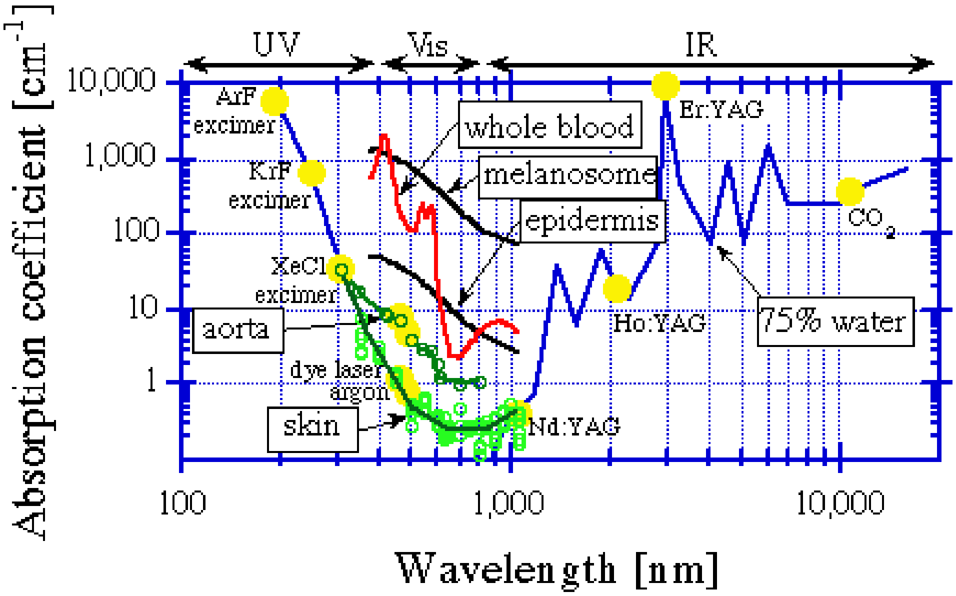

Figure 1.1. Primary absorption spectra of several tissue types and tissue constituents, along with their absorption coefficients at some typical laser wavelengths. Note that the absorption spectra of water has been scaled down by 75% to mimic a typical tissue with 75% water content. From Jacques and Prahl[7].

Optical imaging holds great promise for early cancer detection. Cancerous tissues manifest significant architectural changes at the cellular and sub-cellular levels, which can be detected by the change in their optical scattering properties[9]. Other hallmarks of cancer, such as angiogenesis and hyper-metabolism, directly alter the optical absorption properties of the tissue[10]. Optical imaging can also be used to measure the oxygen saturation of hemoglobin, which is closely related to the metabolic state of tissues and is an important diagnostic parameter.

However, the imaging resolution of pure optical imaging is significantly limited by the strong optical scattering in biological tissues, which are optically turbid media. A typical value of the scattering coefficient for visible light in biological tissues is 100/cm, as compared to 0.2/cm for X-rays used in medical diagnosis[4]. Scattering causes light to change its direction, and multiple scattering causes light to completely lose its original direction.

1.1.2 Diffuse Optical Imaging

Depending on the degree of scattering, light transmitted through tissues can be classified into three types: ballistic light, quasi-ballistic light, and diffuse light. Ballistic light experiences no scattering and carries direct imaging information. Quasi-ballistic light experiences minimal scattering and carries some imaging information. Diffuse light follows tortuous paths and carries little direct imaging information.

Accordingly, optical imaging techniques are classified into two types: ballistic imaging and diffuse imaging. In ballistic imaging, diffuse light is rejected and ballistic or quasi-ballistic light is collected. Time-gated optical imaging[11-13] and optical coherence tomography[14, 15] are examples of ballistic imaging. Ballistic imaging is suitable only for thin tissue samples; for thick tissues with strong light scattering, it suffers loss of signal and resolution. Diffuse optical imaging has been developed for thick tissues to overcome the light scattering limitation. In diffusive optical imaging, diffused light is detected as the imaging signal, and sophisticated image reconstruction algorithms are applied based on diffusion equations or transport equations. Frequency domain optical imaging[16] and DC-based diffuse tomography[17] belong to the diffusive imaging category. The image quality of diffusive imaging is usually algorithm-dependent, and the image resolution is limited.

To further improve the imaging resolution in tissues over several millimeters thick, researchers have developed hybrid techniques that combine the optical and ultrasonic techniques, taking advantage of the negligible acoustic scattering (compared with optical scattering) in soft biological tissues. In the hybrid imaging techniques, the ultrasonic wave carries the spatial information. Hybrid imaging techniques include photoacoustic imaging[18-20], sonoluminescent tomography[21], and ultrasound-modulated optical tomography (UOT)[22]. This thesis focuses on the development of UOT.

1.1.3 Ultrasound-modulated Optical Tomography (UOT)

In UOT, a focused ultrasonic wave is used to modulate the diffused coherent light inside the biological tissues. The ultrasonically modulated or encoded photons are frequency shifted by the ultrasonic frequency, and can be discriminated from the un-modulated background light. The ultrasonic focus carries the spatial information and determines the spatial resolution for the ultrasonically modulated photons[23]. Thus, by providing optical contrast and ultrasonic resolution, UOT combines the advantages of ultrasound imaging and optical imaging. Because of these intrinsic characteristics, it is well suited for soft tissue imaging.

UOT holds promise for broad applications in biomedical diagnosis, such as breast cancer and skin cancer detection. However, there remain challenges in UOT's theoretical understanding and practical applications. For example, in practice, the sample thickness in breast cancer diagnosis will be 5-10 cm. For UOT imaging in such thick tissue, signal detection becomes a critical bottleneck. New development is required to improve the sensitivity of the signal detection techniques. In addition, the detection configuration should be modified to meet the requirement of convenience for practical applications.

1.2 Signal Detection in UOT

In UOT, the signal light is modulated by a focused ultrasonic wave, which can be modeled as phase modulation at the ultrasonic frequency. When expanded in the frequency domain, the signal light contains several parts: the unmodulated light has the original optical frequency ν_0, while the ultrasonically modulated light has frequencies shifted from the optical frequency by multiples of the ultrasonic frequency, *i.e.*, $\nu_0 \pm n f_a$, where n is an integer and f_a is the ultrasonic frequency. In the weak modulation approximation that is usually the case, all the higher harmonics are negligible except the first order terms $\nu_0 \pm n f_a$. One of these two sidebands is usually detected as the signal for

UOT imaging[24-26].

The signal-to-noise ratio (SNR) of UOT is limited by several factors. First, the number of the diffuse photons being modulated by a focused ultrasound beam inside a turbid medium is overwhelmed by the un-modulated, background diffuse photons, which results in a small degree of modulation. Second, as a coherent light beam scattered through a turbid medium, the wave front of the diffused light becomes speckled, which limits the coherence detection to single speckles. If multiple speckles were detected, the measured effective modulation depth would decrease as the number of speckles increase[24]. Further more, due to their independent statistical nature[27], the two speckled wave fronts, one of the modulated photons and the other of the un-modulated photons, do not coincide with each other, therefore the heterodyne mixing of the two wave fronts on the detector further deteriorates the SNR. Third, the speckled wave front of the diffused light through biological tissue is not stationary due to various internal motions, such as Brownian motion and internal transportation of microstructures such as blood cells. This usually imposes a speckle decorrelation time τ_C of less than several hundred milliseconds on the UOT signal, which limits the coherent detection time and further deteriorates the signal-to-noise ratio.

In the first part of the thesis, I explore two emerging detection techniques to address the SNR problem in UOT, namely photorefractive detection and spectral-hole burning aided detection,.

1.2.1 Photorefractive Detection for UOT

Chapter 2 presents a study on photorefractive detection for UOT, using $Bi_{12}SiO_{20}$, a commercially available photorefractive crystal (PRC), and a focused ultrasound transducer with 1 MHz central frequency.

Photorefractive crystals produce a local light-induced change in their optical refractive indices when the crystals are under spatially non-uniform illumination. There are two underlying physical properties common to all photorefractive crystals that contribute to photorefractivity: such crystals are both photoconductive and electro-optic.

The working mechanism of the photorefractive effect can be explained as a series of physical processes (see Fig. 1.2) dynamically taking place in response to a non-uniform light illumination[28, 29], e.g., a set of grating patterns resulting from two plane-wave beams interfering, which results in the formation of a non-uniform spatial distribution of the refractive index inside the photorefractive crystal, with a pattern similar to that of the illumination.

Photorefractivity begins with the generation of free charge carriers, such as electrons, that are excited by the light illumination from the valence band to the conduction band. A spatially-varying illumination pattern results in a similarly spatially-varying photogeneration rate, i.e., the photogeneration rate is locally a maximum at the positions of maximum intensity. The nonequilibrium free charge carrier densities lead to charge migration, either by diffusion, or by drift, or both. When no external electric field is applied, the carriers diffuse away symmetrically from the intensity maxima. When an external electric field is present and dominates the internal field, then drift dominates the charge transport. In any case, the transport will separate free charge carriers under the spatially non-uniform illumination.

Further, the free charge carriers will get trapped at defect sites that are available (empty) in the transport process. The immediate consequence of separated and trapped space-charges is the formation of space-charge electric fields. When drift dominates the transport under a large applied electric field, the electric field reaches maxima in the dark fringes, and minima in the bright fringes. The electric field is therefore coincident with the maxima and minima of the intensity pattern. On the other hand, when diffusion dominates the transport process, the electric field maxima are shifted by a quarter fringe spacing. The location of the electric field inside the material, relative to the location of the interference fringes, plays a fundamental role in photorefractive nonlinear optical mixing, such as two-wave mixing.

The final stage of the photorefractive grating formation process is the conversion of the internal space-charge electric field into a spatial modulation of the refractive index of the material. This conversion is made possible by the linear electro-optic effect, or the Pockels effect, where electric field change the refractive index of an electro-optic material. Therefore, the spatially modulated light intensity incident on a photorefractive material is converted through the photorefractive process into a spatial modulation of the refractive index with the same spatial frequency as the intensity pattern. A quarter fringe spacing shift of the refractive index relative to the optical stimulus (for diffusion-dominated transport) has special properties during photorefractive wave mixing. It allows one of the interfering beams to gain intensity at the expense of the other beam. This nonreciprocal energy transfer, or photorefractive gain, is the basis of many photorefractive phenomena and applications.

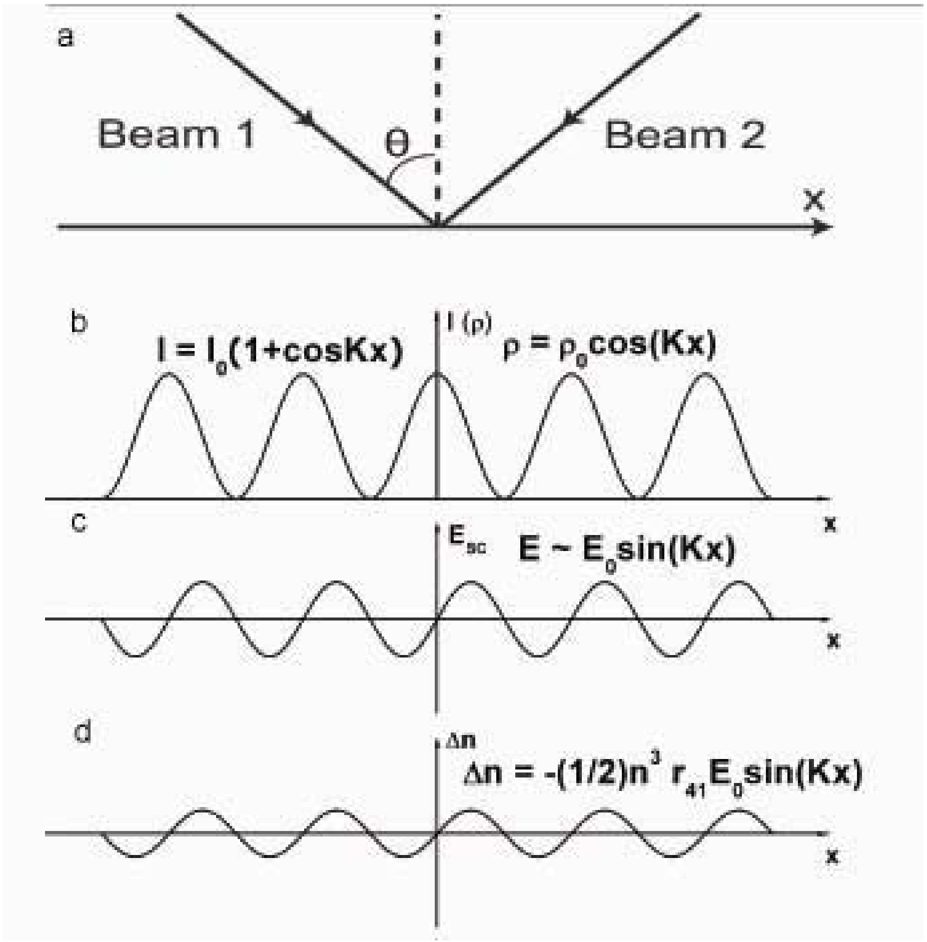

Figure 1.2. The photorefractive effect takes place through a series of dynamic processes. (a) Two plane wave beams incident on a PRC. (b) Interference grating formed by the light illumination. (c) Formation of space-charge field due to diffusion of the photon-generated free charge carriers. (d) Formation of index grating via the linear electro-optic effect (the Pockels effect).

Photorefractive detection makes use of photorefractive two-wave mixing that involves two light beams: the signal beam, which is the diffused signal light from a scattering medium, and the reference beam, also called the pump beam, which is directly derived from the laser source. In photorefractive detection, the PRC is used as an adaptive beamsplitter, in which the signal beam is mixed with the reference beam. This mixing forms an interference grating pattern in the crystal volume. Due to the photoconductivity of the PRC, in the bright regions of the interference grating, light excites more free charge carriers than in the dark regions. Thus, the free charge carriers drift or diffuse from the bright regions to the dark regions; this leads to the formation of a space-charge field, the strength of which spatially follows the illumination interference pattern.

As discussed earlier, the refractive index of the PRC is directly modulated by the local space-charge field. Thus, the light modulated space-charge field in the PRC produces a refractive index grating that also follows the illumination interference pattern. As a result of the quarter fringe spacing shift of the index grating pattern from the illumination pattern due to the diffusion-dominant charge transport in BSO, the reference beam is diffracted from this refraction index grating into the signal beam direction in the two-wave mixing process.

The wave front of this diffracted reference beam replicates that of the signal beam, which provides a local oscillator (LO) important for interferometric detection.

The PRC is adaptive in that the index grating is “rewritten” continually on the time scale of the PRC response time, while the high frequency modulation produced by the ultrasonic source is not compensated for. This adaptivity offers the ability to spectrally filter the un-modulated component in the signal light because the frequency of the reference light is identical to that of the ultrasound-modulated component. Furthermore, any slow variation of the wavefront in the signal beam due to speckle decorrelation can be compensated for by the dynamically refreshed index grating, provided that the speckle decorrelation time is within the response time of the PRC.

Based on the principle of photorefractive detection, I developed a time-resolved detection scheme using a millisecond-long ultrasound burst, and then imaged both the optical and mechanical properties of biological tissues. This scheme improved the detection efficiency of the ultrasound-tagged photons.

My experiments in both tissue-mimicking phantoms and in chicken breast tissue showed that over an imaging depth of 40 mm, both the optical and acoustical heterogeneity can be resolved at a resolution of ~2 mm, which is determined by the focal width of the ultrasound transducer. Furthermore, because the optical and mechanical properties of tissue have different characteristic time scales, they can be differentiated by analyzing the temporal evolution of the UOT signals.

In chapter two and chapter three, we explore two emerging detection techniques to address the SNR problem in UOT, photorefractive detection and spectral-hole burning aided detection,. In chapter two, we present a study on photorefractive detection for UOT, using $Bi_{12}SiO_{20}$ (BSO), a commercially available photorefractive crystal (PRC), and a focused ultrasound transducer with 1 MHz central frequency. In photorefractive detection, the PRC is used as an adaptive beamsplitter, in which the diffused signal light from a scattering medium is mixed with a reference beam (or pump beam) which is directly derived from the laser source. An interference pattern is formed in the crystal, exciting free charge carriers in the bright regions which drift or diffuse to the dark regions and leading to a space-charge field formation. The index of refraction is modulated through the electro-optic effect, and the reference beam is diffracted off this grating into the signal beam direction in the two-wave mixing process. The wave front of the diffracted reference beam replicates that of the signal beam, providing a local oscillator (LO) for interferometric detection. The diffracted reference beam and the transmitted signal beam interfere at the photodetector, where any phase modulation encoded on the signal beam is converted to an intensity modulation which is observed at the detector. The PRC is adaptive in that the index grating is continually “rewritten” on the time scale of the PRC response time, while high frequency modulation produced by the ultrasonic source is uncompensated. Thus we can spectrally filter the un-modulated component in the signal light when the frequency of the reference light is identical to that of the ultrasound-modulated component. Based on photorefractive detection, we developed a time-resolved detection scheme with a millisecond long ultrasound burst capable of imaging both the optical and mechanical properties of biological tissues, with improved detection efficiency of the ultrasound-tagged photons.

Our experiments in tissue mimicking phantoms and in chicken breast tissue showed that through an imaging depth of 40 mm, both optical and acoustical heterogeneity can be resolved at a resolution of ~2 mm, as determined by the focal width of the ultrasound transducer. Furthermore, the optical and mechanical properties of tissue can be differentiated through analysis of the temporal evolution of the UOT signals because of the difference in the characteristic time scales.

1.2.2 Spectral-hole Burning Aided Detection for UOT

In chapter three, we present a study on a spectral-hole burning (SHB) aided detection in UOT to image optical heterogeneities in thick tissue-mimicking phantom samples and chicken breast tissue. With this detection technique, an SHB crystal is used as a front-end absorptive spectral filter to selectively transmit the frequency component in the diffused light which corresponds to the ultrasound-modulated light, while suppressing all the other frequency components. Being able to process multiple speckles simultaneously while remaining immune to the speckle de-correlation, SHB detection offers a greatly increased etendue compared to the other detection techniques in UOT. In our study, the efficiency of SHB was improved by using a Tm3+: YAG crystal of higher doping concentration (2.0 atomic%) and a double-pass pumping configuration, in which the pump beam was transmitted through the crystal twice, to burn a deeper spectral-hole with the available optical intensity. With the improved SHB-UOT system, we imaged absorbing, scattering, and phase contrast objects that were embedded in the middle plane of a 30-mm thick phantom sample. The imaging resolution was 0.5 mm in the lateral direction, as defined by the focal width of the ultrasonic transducer, and 1.5 mm in the axial direction, as determined by the ultrasonic burst length. We also imaged two absorbing objects embedded in the middle plane of a 32-mm thick chicken breast sample. The results suggest that the improved SHB-UOT system is one step closer to a practical optical imaging application in biological and clinical studies.

1.3 Time-reversed ultrasonically encoded (TRUE) optical focusing

One of the fundamental difficulties in optical imaging of soft biological tissue comes from the fact that multiple scattering of light in turbid media randomizes the light propagation directions within one transport mean free path[30], which prevents effective light focusing in depths beyond this range. This randomization makes it difficult to use light as an imaging probe to "see" deep into a turbid medium or to deliver light for light-matter interaction at specific sites inside the medium.

To overcome the depth limitation of optical focusing, or in general, of light propagation in turbid media, a variety of approaches have been explored. The turbidity of a scattering medium can be artificially reduced by optical clearing[31, 32], which matches the refractive indices of the scatterers in a scattering medium with that of the ground material by introducing optical clearing agents into the medium. This improves the optical penetration depth and imaging contrast, while it alters the optical properties of the medium, which is not always desirable or applicable. Without extraneous control of its optical properties, the turbidity of a scattering medium can be suppressed by optical phase conjugation (OPC) in a two-pass configuration[33]. The usefulness of this method is limited to imaging objects through a diffuse layer, but not inside such layer. Nor is it helpful in focusing light inside a diffuse medium. Another approach to achieve light focusing inside[34] or through[35] a turbid medium, without changing its optical properties, is to adaptively shape the wavefront of the incident light through a feedback loop. The feedback mechanism, however, requires the presence of a guide star—a luminous point—for the incident light to be focused on. In addition, the time it takes for the iterative feedback algorithm to find the optimal incident wavefront is on the order of several minutes, much longer than the millisecond time scale of the micro structure changes in biological tissue. These factors prevent the technology from being useful in situations where arbitrary, dynamic, or real time light focusing is desired.

To overcome the above restrictions, time-reversed ultrasonically-encoded optical focusing, or TRUE optical focusing is proposed. TRUE is based on the principles of ultrasonic modulation and optical phase conjugation, or OPC, of multiple-scattered coherent light, to dynamically focus light into a scattering medium in a two-pass configuration. In this technique the wavefront of the ultrasonically encoded light emanating from a virtual source (i.e., the ultrasonic focus) inside a turbid medium on the first pass can be restored by OPC on the second pass on the wavelength scale, and will then converge to the virtual source. The virtual source, defined by the ultrasonic focus, serves as a virtual guide star. Its size and position are adjustable by the ultrasonic device instead of by optical focusing elements. Thus TRUE optical focusing can invasively focus light to an arbitrary spot defined by the ultrasonic focus inside a turbid medium. Being a diffuse optical method, TRUE optical focusing is insensitive to the optical thickness of the turbid medium and ideally could reach focal depths beyond ten centimeters in a scattering-dominant medium, such as human breast tissue. This modality is presented in Chapter four.

Finally, in Chapter five, we present a summary of this dissertation.

Chapter 2

UOT with Photorefractive Detection

2.1 Optical Imaging and UOT

Optical imaging of soft biological tissue is a non-invasive, nonionizing, and functional imaging modality, which makes it highly desirable in the biomedical field. The photon energy used in optical imaging is typically ~2 eV for λ = 500 nm, which is safe for biological molecules, as compared with the radiation used in X-ray imaging which is ~50 KeV. Because its contrast is based on optical properties (i.e., absorption and scattering) of the tissue, optical imaging can provide better soft-tissue contrast than the ultrasound imaging, which is based on mechanical contrast. Optical absorption and scattering properties in the visible and near infrared wavelengths are intrinsic indicators of tissue abnormalities and functions since they are determined by the molecular constituents of tissues and the electronic and/or vibrational structures at the molecular level. For example, cancerous tissues manifest significant architectural changes at the cellular and sub-cellular levels, which result in changes to the optical scattering properties. Angiogenesis and hyper-metabolism, which are characteristic of cancers, result in changes to the optical absorption properties. Therefore, optical imaging holds great promise for early cancer detection. Other important physiological parameters can also be measured by optical imaging, such as the oxygen saturation of hemoglobin, which makes optical functional imaging possible.

However, pure optical imaging lacks good spatial resolution in deep tissue because of strong optical scattering in the visible and NIR wavelengths. For imaging modalities that detect ballistic or quasi-ballistic photons as imaging signals, such as time-gated imaging and optical coherence tomography, the detected photons experience minimal scattering inside tissues and carry spatial information, but the signal strength decays exponentially with increasing tissue thickness. These imaging modalities are therefore not suitable for deep tissue imaging. For diffuse optical imaging modalities that collect diffused photons transmitted through thick tissues as imaging signals, the diffused light decays more slowly in thick tissues, but the spatial information is lost in diffuse photons because multiple scattering randomizes light propagation after several scattering mean free paths. At $\lambda = 500$ nm, the mean scattering free path $l_s = 0.1$ mm in the human breast, while $l_s = 50$ mm for photons at the X-ray wavelength used in medical diagnosis. In diffuse optical imaging, convoluted image reconstruction is needed to recover the spatial distribution of the relevant optical properties. Since this is usually an ill-posed inverse problem, the image resolution and the image quality are not good.

To take advantage of the high optical contrast and overcome the poor spatial resolution of optical imaging in thick tissues, the use of ultrasound has been explored, which resulted in several hybrid imaging modalities such as photoacoustic imaging and ultrasound-modulated optical tomography (UOT). Because acoustic scattering is 1000 times less than optical scattering in soft biological tissues, ultrasonic waves provide spatial resolution in these hybrid imaging modalities. In UOT, a focused ultrasonic wave is used to modulate the diffused light inside biological tissues. The ultrasonically modulated (or encoded) photons are frequency shifted by the ultrasonic frequency and can be discriminated from the un-modulated background light. The ultrasonic focus determines the spatial resolution for the ultrasonically modulated photons. Thus UOT has the combined advantages of optical contrast and ultrasonic resolution.

In UOT, a focused ultrasound beam interacts with diffused light by means of phase modulation inside a biological sample. The intensity of the ultrasonically modulated (or tagged) light at the detector is proportional to the fluence of the diffused light probed by the ultrasonic wave. By scanning the ultrasound beam through the sample, a tomographic image of the light fluence can be constructed, which can be used to recover the spatial distribution of optical properties which are of biomedical interest.

The development of UOT has been chronicled by the development of its signal detection methods (Table 1). When ultrasound modulation of diffused light was first experimentally demonstrated by Marks *et al.*[36], a single element detector (photomultiplier) and Fabry-Perot interferometer were used for signal detection in the time and spectral domain. Leveque *et al.*[37] implemented a parallel speckle detection method to improve the signal to noise ratio (SNR), where a CCD camera was used as a detector array with a source-synchronized lock-in technique. Sakadzic and Wang[38] used single ultrasound pulses and a confocal Fabry-Perot interferometer to obtain microscopic UOT images in biological tissues, with resolution scalable to ultrasound wavelength (<100um) at imaging depths > 3mm. Murray *et al.*[39] used a photorefractive crystal (PRC) based detection system to enhance the detection efficiency.

Table 2.1 Different signal detection methods in UOT.

Detection methods	**Main features**	**First reported by**
Single element detector (photo diode, PMT, etc.)	Single speckle grain; real time response; photon starving	Leutz W. *et al.*,[40] Wang L. V. *et al.*,[22] Kempe M. *et al.*[24]
Parallel detection (CCD)	Parallel detection of multiple speckle grains; improved etendue; slow exposure speed; photon starving	Leveque S. *et al.*[37]
Fabry-Perot interferometer	Spectral filtering; immune to speckle; small etendue; slow speed	Leutz W. *et al.*,[40] Sakadzic S. *et al.*[38]
Photorefractive detection (photorefractive material)	Adaptive, dynamic beam splitter; increased etendue; spectral filtering;	Murray T. W. *et al.*[39]
Spectral-hole burning (SHB crystal)	Spectral filtering; largest etendue;	Li Y. *et al.*[41, 42]

The development of UOT signal detection methods has pursued improved SNR and system etendue, difficulties in UOT that are inherently related to the mechanism of ultrasonic modulation of coherent laser light in a scattering medium[25, 43]. First, because the ultrasonic focal volume is small compared to the entire light diffusion volume, the modulation depth *m*—defined as the ratio of the ultrasound-modulated light intensity to the un-modulated light intensity—is low. Second, multiple scattering results in a speckled wavefront of the diffused light. The average grain size of the speckle sets the upper limit of the spatial coherence area when both of the ultrasound-modulated and un-modulated components fall on the photodetector surface. For a single speckle grain, the heterodyne mixing of the two components has an etendue < λ^2 (where λ is the light wavelength) because the two wavefronts are not perfectly matched since the two components follow independent statistics in diffusion[44]. When the detector surface is large compared to the average speckle grain size (~λD/L, where D is the dimension of the light emanating surface, and L is the distance between the source and the detector), multiple speckle grains will be integrated, which results in a reduced effective modulation depth $m_{eff} = \langle m \rangle / \sqrt{N}$ [24], where N is the number of grains. This reduction leads to a trade-off between the measured m_{eff} and the system etendue, which can be defined as $G = \iint_{\Omega,S} d\Omega dS$, where $d\Omega_S$ is the solid angle subtended by the light emanating surface when viewed from the surface element dS of the detector. A system with an improved etendue will collect more signal light, but will result in a decreased m_{eff} because of an increased number of speckle grains *N*, and vice versa. An additional complication in the *in vivo* imaging of biological tissue is the speckle decorrelation caused by internal movement of the scattering medium such as Brownian motion. This movement limits the coherence detection time to within the speckle decorrelation time of the tissue, usually on the order of 1 – 100 milliseconds.

2.2 $Bi_{12}SiO_{20}$ Photorefractive Crystal

In recent years, photorefractive crystal (PRC) based detection has been applied to UOT, and has effectively improved the etendue of the imaging system. The improvement capitalizes on PRC's real time holography ability in a two wave mixing (TWM) scheme. PRC's are a group of materials that exhibit both photoconductive and electro-optic properties[45, 46]. The unique photorefractive feature makes PRC suitable for many applications, including coherent signal detection, optical image processing, real-time holography, and others[47-49]. Several variations of the PRC-based UOT system have been implemented, and the relevant theories have been developed by various groups[50-53].

$Bi_{12}SiO_{20}$ (BSO), a sillenite photorefractive crystal, is a cubic oxide crystal of the sillenite family. It belongs to the cubic noncentrosymmetric crystal point group 23, i.e., the crystal structure is symmetric for 180° rotations about the crystal axis and 120° rotations about the diagonals of the cube. It is piezo-electric, electro-optic, elasto-optic, and optically active[54].

In comparison to other commonly used PRC's, such as $BaTiO_3$ and GaAs, BSO has much smaller electro-optic coefficient, similar mobility, and smaller dielectric constant. However, it has larger photoconductivity, which leads to better sensitivity. Table 2.1 lists the material parameters for $BaTiO_3$, BSO, and GaAs[55].

Table 2.2 Materials parameters for $BaTiO_3$, BSO and GaAs

Material class	Ferroelectric oxide	Sillenite	Compound semiconductor
Material	$BaTiO_3$	BSO	GaAs
Photorefractive Wavelength (μm)	0.4 – 1.1	0.45 – 0.65	0.9 – 1.3
Electro-optic coefficient e_{eff} (pm/V)	100 (r_{33}) 1640 (r_{42})	4 (r_{41})	1.4 (r_{41})

Dielectric constant	135 (r_{33}); 3700(r_{11})	56	13.2
$n_b^3 r_{eff}/\varepsilon$ (pm/V)	10 (r_{33}); 6(r_{42})	1.4	3.3
Mobility μ (cm^2/V-s)	0.01	0.1	6000
Recombination time τ_r (s)	10^{-8}	10^{-6}	3×10^{-8}
Diffusion length L_d (μm)	0.01	0.5	20
Photoconductivity $\mu\tau_r$ (cm^2/V)	10^{-10}	10^{-7}	1.8×10^{-4}

Table 2.3 lists the relevant physical parameters of BSO at three wavelengths:

Table 2.3. Physical parameters of BSO[56]:

Parameter	λ = 488 nm	λ = 514.5 nm	λ = 632.8 nm
Refractive Index n	2.650	2.815	2.530
Absorption α (cm^{-1})	7.0	2.8	0.6
Optical rotatory power ϱ (°/mm)	45.5	38.6	21.4
Photon ionization energy E ($\times10^{-12}$ erg)	4.07	3.88	3.14
Dark resistivity R (Ω-cm)	5×10^{13}		

Figure 2.1 shows the crystallographic structure of BSO and the experimental configuration of the crystal.

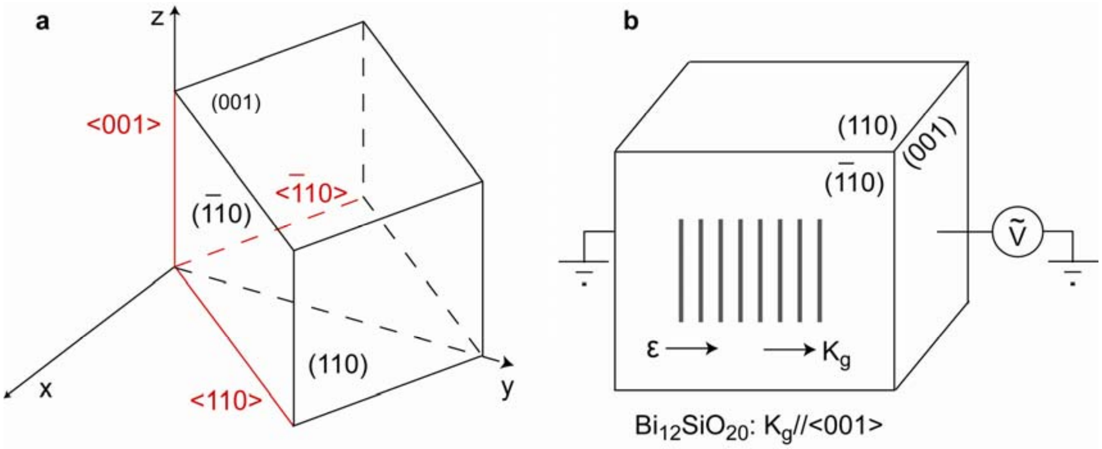

Figure 2.1. $Bi_{12}SiO_{20}$ photorefractive crystal. (a) Crystal orientation and its crystallographic axes x, y, and z. (b) A high voltage square wave electric field is applied on the two (0 0 1) faces of the crystal to enhance the wave mixing and holographic recording efficiencies. Both the signal and pump light beams are incident on the (-1 1 0) face.

2.3 Experimental Methods

We constructed a PRC-based UOT system with a quasi-continuous wave (CW) ultrasound modulation scheme, where a one-millisecond long focused ultrasound burst was applied to the sample and the time-dependent change of the detected optical signal was recorded to image both the optical and mechanical properties of the sample. The benefits of using a millisecond long ultrasound burst are two-fold: it improves the SNR; and it also enables the detection of the effects of the acoustic radiation force, which happens in milliseconds and can be related to the mechanical properties of the sample.

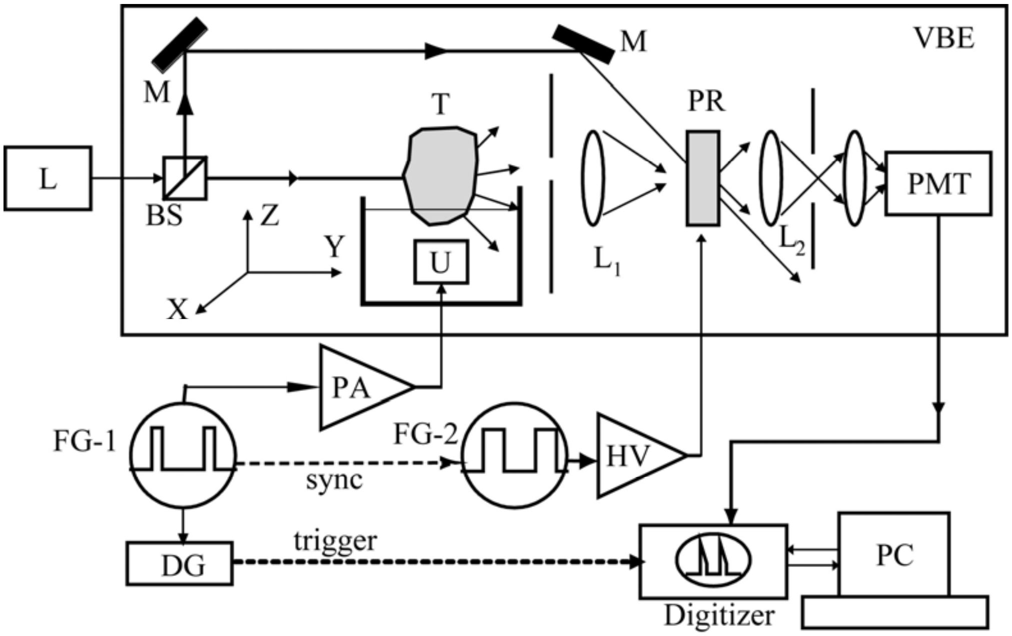

Figure 2.2. Schematic of the experiment setup: L, laser; BS, beam splitter; M, mirror; L$_1$, L$_2$, lens; PR, photorefractive crystal BSO; PMT, photomultiplier; FG-1, FG-2, function generators; PA, power amplifier; DG, pulse-delay generator; HV, high voltage amplifier; PC, personal computer; U, 1 MHz ultrasound transducer; T, study sample; VBE, vibration block enclosure; Digitizer, GAGE CompuScope 14200 14 bit waveform digitizer.

Our experiment setup, shown in Fig. 2.1, was similar to that proposed by Murray *et al.*[50]. The light from a Coherent Verdi laser (λ= 532 nm) was split into two paths: one (signal) for illuminating the sample and the other for pumping in two-wave mixing in the photorefractive crystal. The sample was insonified by a focusing ultrasonic transducer (Ultran Lab VHP100-1-R38) with a central frequency of 1 MHz, focal length of 37.5 mm, focal zone length of 23 mm and focal spot diameter of 2.2 mm. The peak acoustic pressure at the focus was 1.5 MPa. The high amplitude of the ultrasound burst was compensated by its low duty cycle (burst rate was 100 Hz) so that the ultrasound safety limit was still satisfied[57]. An alternating electric field (1 kHz, 4 kV) was applied to the BSO crystal to enhance the TWM gain. The pump light intensity incident on the BSO was kept around 10 mW/cm^2. Under this condition, we confirmed that the crystal response time was at least 100 ms, which was comparable to the speckle de-correlation time of 2 cm thick *ex vivo* chicken breast tissue[58]. The system was enclosed in an acrylic enclosure to protect the real time holography from ambient perturbation.

2.4 Results and Discussions

To quantify the improvement of UOT signal strength with increasing ultrasound burst duration, a phantom sample (sample #1) of 10×4×10 cm (X×Y×Z) outer dimensions was prepared with 10% porcine gelatin and 1% Intralipid concentration, resulting in a reduced scattering coefficient $\mu_s' = 10\text{cm}^{-1}$. Ultrasound bursts consisting of various numbers of cycles were applied to the phantom, and light intensities after the BSO were registered by the photomultiplier. The signal strength was defined as the change in detected light intensity with and without ultrasound modulation. Figure 2.2 shows the signal increase and saturation as the ultrasound burst length increases. Several possible mechanisms can account for this: 1). The increasing ultrasound burst duration fills a larger sample volume along the Z axis, which increases the amount of ultrasound-modulated light at the expense of axial resolution; 2). The momentum transfer in the ultrasound focal zone increases with the increasing ultrasound duration due to the radiation force effect[59], which increases the ultrasound modulation of light in the focal zone; 3). The TWM response time in BSO due to the intensity change of the un-modulated light is comparable to this time scale.

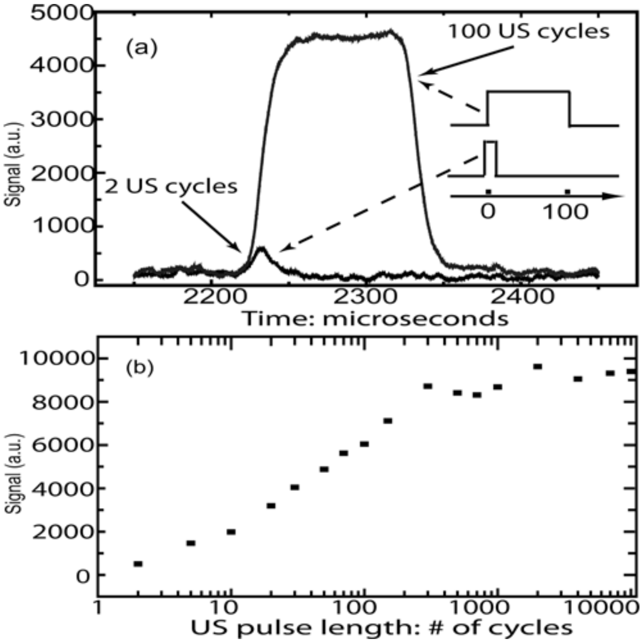

Figure 2.3. (a) Signal intensity comparison between a short ultrasound burst (2 cycles) and a long one (100 cycles). (b) Signal intensity grows as the burst length increases.

We took advantage of the higher signal levels provided by the long ultrasound burst to image chicken gizzard pieces embedded in chicken breast tissue (sample #2) (Fig. 2.3). The two chicken gizzard pieces, each 6×6×10 mm, were separated 10 mm apart inside an 8×2.5×3.8 cm chicken breast sample, which was buried in 10% porcine gel with the same outer dimensions as sample #1. Chicken gizzard has higher optical absorption than the surrounding chicken breast tissue but similar mechanical properties. This difference translates into less ultrasound-modulated light inside the chicken gizzard, hence less change of the un-modulated light, and a decrease in the UOT signal. This decrease was illustrated by two dark troughs at the locations of the two gizzards, as seen in the 2D images in Fig. 2.3.

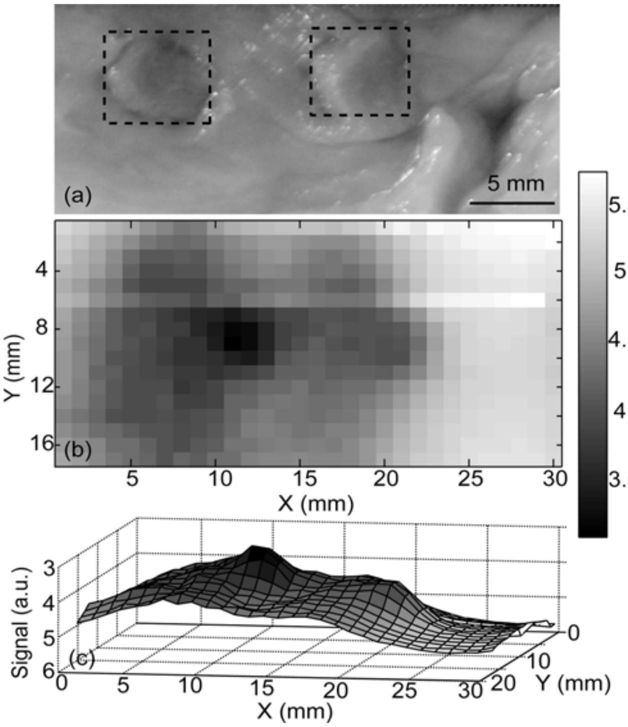

Figure 2.4. UOT image of sample #2. (a) Picture of the sample; (b) and (c) density and surface maps of the 2D UOT image of (a); the surface map is upside down to show the objects.

To demonstrate imaging based on mechanical properties rather than optical properties, a phantom sample (sample #3) was prepared with the same composition and outer dimensions as sample #1. Two 6 mm cubic volumes enhanced with 20% corn starch were buried inside with a 12 mm separation. The two inclusions had minimal differences in optical properties, but higher mechanical contrast than the background. As a result, the inclusions were barely discernible in the UOT image acquired 0.1 ms after the onset of the ultrasound burst (Fig. 2.5, upper plot), but markedly visible on the image acquired 0.1 ms after the passage of the ultrasound burst (Fig. 2.5, lower plot). The mechanical property differences gave rise to the acoustic radiation force effect that happens on a time scale of several milliseconds[59].

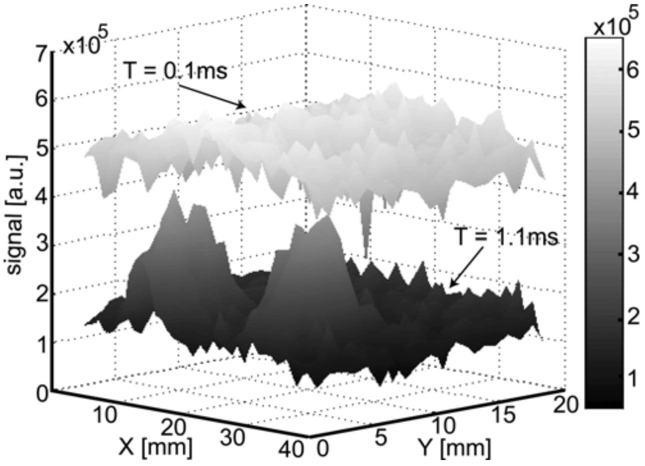

Figure 2.5. UOT surface maps sample #3 at T = 0.1 ms and 1.1 ms after the start of a 1-ms long ultrasound burst.

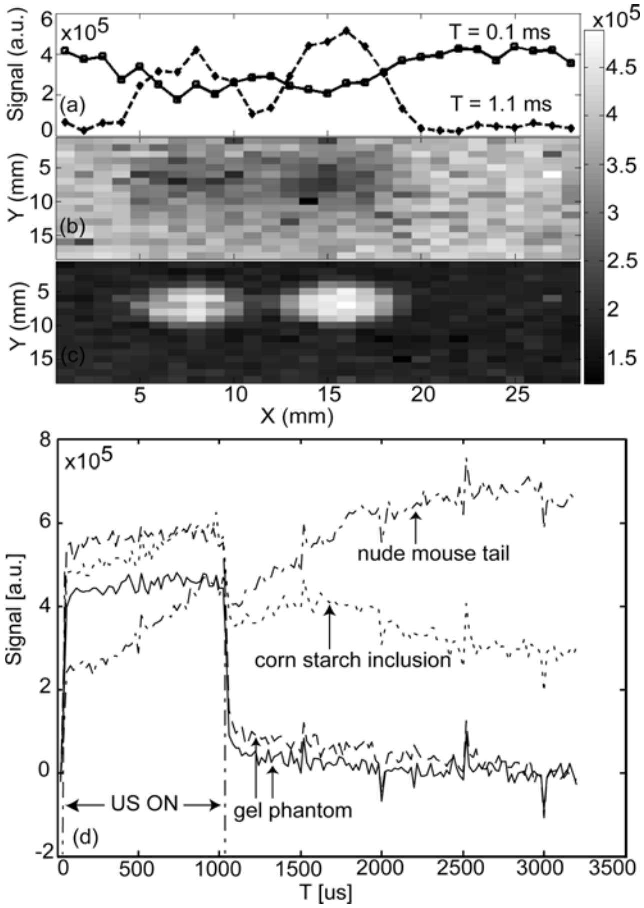

Figure 2.6. (a). 1D scan at y = 7 mm of sample #4; (b). 2D density map at T = 0.1 ms and (c) T = 1.1 ms; (d). comparison of time-resolved UOT signal for different objects.

We next demonstrated UOT imaging based on both optical and mechanical properties by imaging two 3×10 mm (diam.×Z) segments of nude mouse tail 8 mm apart and embedded in a gelatin sample (sample #4) with the same composition and outer dimensions as sample #1. The UOT image (Fig. 2.6(b)) acquired at T = 0.1 ms after the onset of the ultrasound was mainly based on optical absorption contrast. Owing to the higher absorption of the mouse tails, they appear dark, but the contrast is low. The image quality is much better using ultrasound light modulation produced by the radiation force effect, due to the large acoustic impedance mismatch between the bone structures of the nude mouse tail and the background gelatin phantom. This improvement is shown in Fig. 2.6(c), where the image was acquired 0.1 ms after the end of the 1 ms ultrasound. Here the mouse tails appear bright due to strong acoustic modulation. The 1D scans (Fig. 2.6(a)) across the sample at the two different times show the different effects of optical and mechanical contrasts on the UOT signal.

Details of the mechanical properties of the object, such as the acoustic impedance mismatch, can be characterized from the time evolution curves of the UOT signal. To demonstrate this, a comparison of time-evolution curves from the nude mouse tail, the corn starch inclusion, and their background gelatin phantoms is shown in Fig 2.6(d). For the nude mouse tail, the radiation force effect kept increasing long after the ultrasound was turned off, while for the corn starch inclusion it started decay 0.5 ms after the end of the ultrasound burst. For both samples, the background gelatin curves showed little radiation force effect, as expected. Separation of the sample's mechanical and optical contrast is possible once the acoustic impedance can be derived from the time-resolved UOT imaging.

2.5 Conclusion

In summary, this study has demonstrated that both the optical and the mechanical properties of a sample can be detected with a millisecond ultrasound burst, using PRC-based UOT. Time gating the optical signal even allows decoupling of the optical and mechanical information from UOT. Finally, the SNR can also be improved with a longer ultrasound burst.

Chapter 3

UOT with Spectral-hole Burning Detection

3.1 Spectral-Hole Burning for UOT

Spectral-hole burning (SHB), one of the latest detection methods in UOT, offers great promise in improving the signal detection with little sacrifice, thereby advancing this imaging modality closer to practical application.

SHB has been extensively investigated for various applications[60-62]. An SHB crystal is a rare-earth ion doped, inhomogeneously broadened optical absorber, which can be modeled as a two-level atomic system[63]. When cryogenically cooled, it has a sub-MHz homogeneous linewidth $\Delta\Gamma_H$ and a GHz inhomogeneous bandwidth $\Delta\Gamma_I$. Each homogeneous frequency within $\Delta\Gamma_I$ can be individually accessed using properly tuned narrow laser line excitation. When pump beam from a monochromatic laser source at frequency ω_P , with intensity I_P , illuminates a cryogenically cooled SHB crystal, ions having excitation frequency ω that is nearly resonant with the pump beam absorb the photons and are then excited from their ground states, yielding a spectral-hole in the crystal's absorption band[62-65]. As a consequence, the corresponding absorption coefficient $\alpha(\omega_P, z)$ is reduced.

To improve the detection efficiency of UOT, it was recently proposed to use an SHB crystal as front-end absorptive filter[41, 42]. The use of this filter circumvents the spatial and temporal coherence limit in detecting the speckled wavefront by selectively passing the modulated light while suppressing all of the other spectral components. In the ideal case, all SHB-filtered photons are ultrasonically encoded ones; thus, the speckle grains can be added in terms of intensity, although the filtered wavefront of the modulated light is still speckled. Compared with the other detection techniques for UOT, SHB detection has the advantage of a higher etendue, and therefore can detect more modulated light, which becomes increasingly critical in imaging thicker tissues. The applicability of SHB in UOT was experimentally demonstrated with imaging results from 10-mm thick biological-tissue-mimicking phantom samples[41, 42].

Here, we report more experimental results as we further explore the potential of SHB for UOT imaging of thicker biological tissue. To improve the SHB efficiency, we implemented a double-pass pumping scheme, which resulted in deeper spectral-holes with the available pump-beam intensity. The enhanced imaging ability was demonstrated by differentiating the absorbing, scattering, and phase objects in a 30-mm thick tissue-mimicking phantom with good lateral and axial resolutions. High resolution images of absorbing objects embedded in the middle of a 32-mm thick chicken breast tissue were also obtained. These results advance SHB-UOT one step closer to optical imaging in biological and clinical studies.

3.2 Experimental Methods

3.2.1 Tm^{3+}: YAG crystal used in SHB

The SHB crystal used in our experiment was a 2.0-atomic%-doped Tm^{3+}:YAG crystal, with dimensions of $10 \times 9 \times 2.5\,mm^3$. It had an absorption peak at $\lambda = 793.38$ nm, corresponding to the $^3H_6 \rightarrow {}^3H_4$ transition of the Tm^{3+} ions (Figure 3.1) at temperatures below 4.7 K. When cryogenically cooled below 4.7 K, the crystal showed an absorption peak at $\lambda = 793.38$ nm, corresponding to the $^3H_6 \rightarrow {}^3H_4$ transition of the Tm^{3+} ions[61, 66]. Several factors make the Tm^{3+}:YAG crystal an attractive choice of a narrow-band spectral filter for UOT study: its operating wavelength is in the near-infrared (NIR) region, which is a preferred biomedical imaging window; its inhomogeneous absorption linewidth of 25 GHz is broad enough to accommodate clinical ultrasonic frequencies;

and its homogeneous linewidth of ~150 kHz facilitates effective removal of the un-modulated light. When the crystal is illuminated by a pump beam of a prescribed frequency shift (tuned with an acousto-optic modulator AOM1), a narrow spectral hole is burned within the absorption band. The spectral hole burned by the pump light from a Ti-Sapphire laser in the experiment had a FWHM around 710 kHz, narrow enough to remove the un-modulated light, which was shifted by 5 MHz (the ultrasonic frequency) from the ultrasound-modulated light. The spectral hole's life time is ~10 ms due to the existence of a shelving middle state $^3F_4$[61], which makes it possible in UOT experiments to switch between the burning the spectral hole and detecting UOT signal. During this 10 ms period, the SHB crystal acts as a narrow-band spectral filter by strongly absorbing spectral components of the signal light that are outside of the engraved spectral hole.

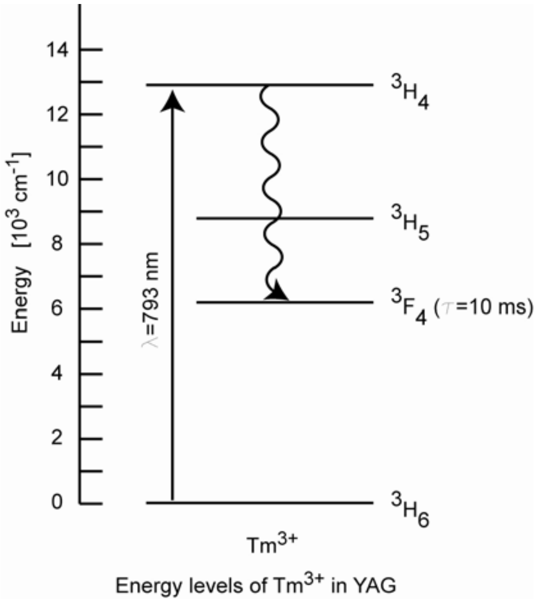

Figure 3.1. Energy transition in Tm^{3+}:YAG corresponding to λ = 793.38 nm absorption.

3.2.2 Experimental Set-up

Figure 3.2 schematically shows our experimental setup for UOT with SHB, whose single-pass version was implemented and described earlier[41, 42]. The Tm^{3+}:YAG crystal was placed in a cryostat, which was installed between the biological sample and the photon detector. The temperature of the crystal was kept below 4.7 K for the duration of the experiment. The pump and the signal light beams were both derived from the same source, a CW Ti:Sapphire laser (Coherent MBR110E), which was pumped by a frequency doubled diode-pumped Nd:YAG laser (Coherent Verdi V10) and operated at 793.38 nm with a linewidth of ~181 kHz and output power of 2 W. Two acousto-optic modulators (AOM, IntraAction AOM 802-A1) worked in combination with an ultrasound transducer to match the frequencies of the pump beam and the ultrasound-modulated light on the signal path. In the experiment, AOM1 was first turned on for 3.3 ms with a 70 MHz sinusoidal RF wave, diffracting light into the first order. This first order beam, used as the pump beam, was then expanded into a 9 mm diameter collimated beam delivering 900 mW optical power. After AOM1 was turned off, AOM2 was turned on with a 75 MHz sinusoidal RF wave, diffracting the incident laser beam into its first order to illuminate the scattering sample. The diffused light inside the sample interacted with a traveling ultrasound burst consisting of five cycles of a 5 MHz sinusoidal wave, which was emitted by a focused transducer (Panametrics-NDT A326S; focal length: 16.2 mm; focal width: 0.5 mm). The interaction generated the ultrasound-modulated component within the signal light exiting the sample. A condensing lens (L5) after the sample then focused the signal light onto the SHB crystal placed inside the cryostat chamber. The modulated component of the signal light was spectrally filtered by the SHB crystal before it was detected by a large area (3.6×3.6 mm^2) photodiode (Thorlabs PDA55). The output signal was fed through a preamplifier (Stanford Research SR560) and coupled into a digitizer (Gage CompuScope 14200) for data analysis.

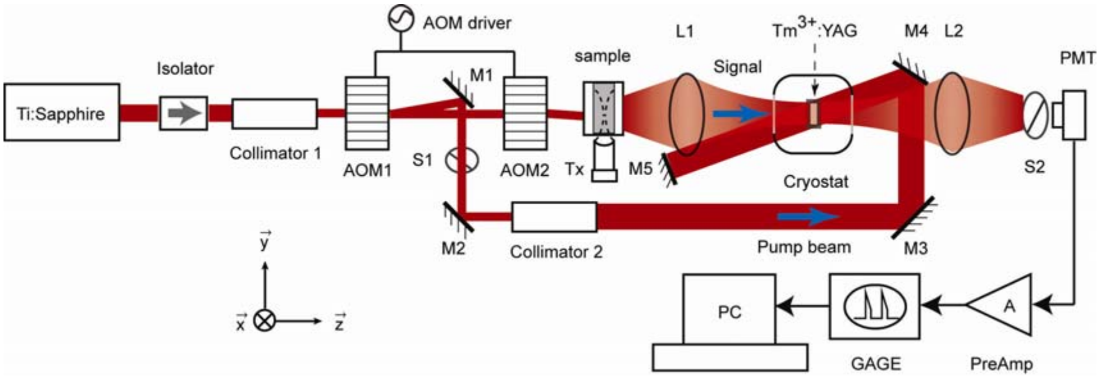

Figure 3.2. Schematic of SHB-UOT experimental setup: Ti-Sapphire laser, Coherent MBR110; L1 - L6, lens; M1 – M5, mirrors; AOM1, 2, acousto-optic modulators; S1, S2, mechanical shutters; Tx, ultrasound transducer; PMT, photomultiplier tube; PreAmp, preamplifier; GAGE, 200MHz data acquisition card; PC, personal computer.

3.3 Results and Discussions

The efficiency of the SHB crystal as a narrow bandpass filter depends on the depth of the spectral hole. To burn a deeper hole with the available optical power, we used a double-pass pumping scheme, where a mirror M5 was placed diagonal to M4 across the cryostat to reflect the pump beam back onto the Tm^{3+}:YAG crystal. To quantify the increase in the spectral-hole depth from the double-pass pumping scheme as compared to the conventional single-pass method, we measured the transmission of a weak probe beam (~15 μW) through the SHB crystal, which was modulated by a five-cycle 5 MHz ultrasound burst when passing through the transducer focus in a clear gelatin phantom. A 38% increase in the transmission efficiency was observed (Fig. 3.3). Assuming the validity of Beer's law $I_{out} = I_{in} exp(-a_0 \cdot L_C)$ and given L_C = 2.5 mm for the thickness of the Tm^{3+}:YAG crystal used in the experiment, we found a reduction of the absorption coefficient $\Delta a_0(\omega_P)$ = 0.13 mm^{-1} at the pump light frequency ω_P due to the increased spectral-hole depth with the double-pass pumping scheme.

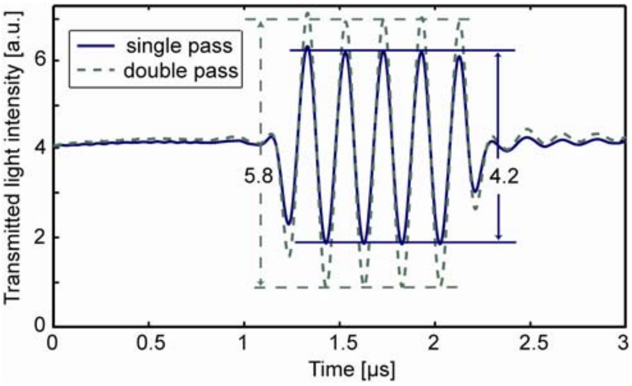

Fig. 3.3. Comparison of the transmitted probe beam powers. The probe beam was modulated by a five-cycle 5 MHz ultrasound burst and filtered by the SHB crystal, when SHB was operated in single-pass and double-pass pumping configurations.

The improvement with the double-pass pumping method suggests that it is possible to burn deeper spectral-holes if higher optical power is available in the laser. In our experiment, a 2.5-mm thick, 2.0-atomic%-doped Tm^{3+}:YAG crystal was pumped by a 900 mW beam with a 9 mm collimated beam diameter for 3.3 ms. As a comparison, in a previous demonstration[66] a 2.5-mm thick, 0.5-atomic%-doped Tm^{3+}:YAG crystal was used as a spectral filter, which was pumped by laser pulses lasting 150 μs, with a typical pulse energy of 450 nJ and a beam waist of 90 μm. The fluence at the crystal surface due to the pump light was 1.5 times as large as that in our experiment. On the other hand, since the doping concentration of our crystal was four times as large, even higher optical power was needed to reach SHB saturation[41] in our experiment. The higher doping concentration of the SHB crystal, while enabling a deeper spectral-hole and hence better spectral filtering, comes at the expense of the increased spectral-hole width, which turned out to be of negligible consequence for our imaging applications.

In the initial studies of SHB-assisted detection in UOT, an imaging experiment was conducted on a 10-mm thick tissue-mimicking phantom sample. To explore its potential in a practical biomedical imaging setting, it is desirable to use SHB assisted UOT to image real biological tissues thicker than 10 mm. With improved detection efficiency resulting from the double-pass pumping scheme and using a higher doping SHB crystal, the deep tissue imaging capability of our SHB-UOT system was put to test with these objectives in mind. The tissue-mimicking samples were prepared by mixing 10-wt.% porcine gelatin (Sigma G2500) and 1-wt.% Intralipid (Fresenius Kabi) in distilled water and molding the solution into slabs of various thicknesses along the light propagation direction. The light incident side of the sample measured 100×60 mm^2. The background samples had a reduced scattering coefficient $\mu_s' = 0.7$ mm^{-1} for the laser wavelength of 793.38 nm and a thickness of 30 mm.

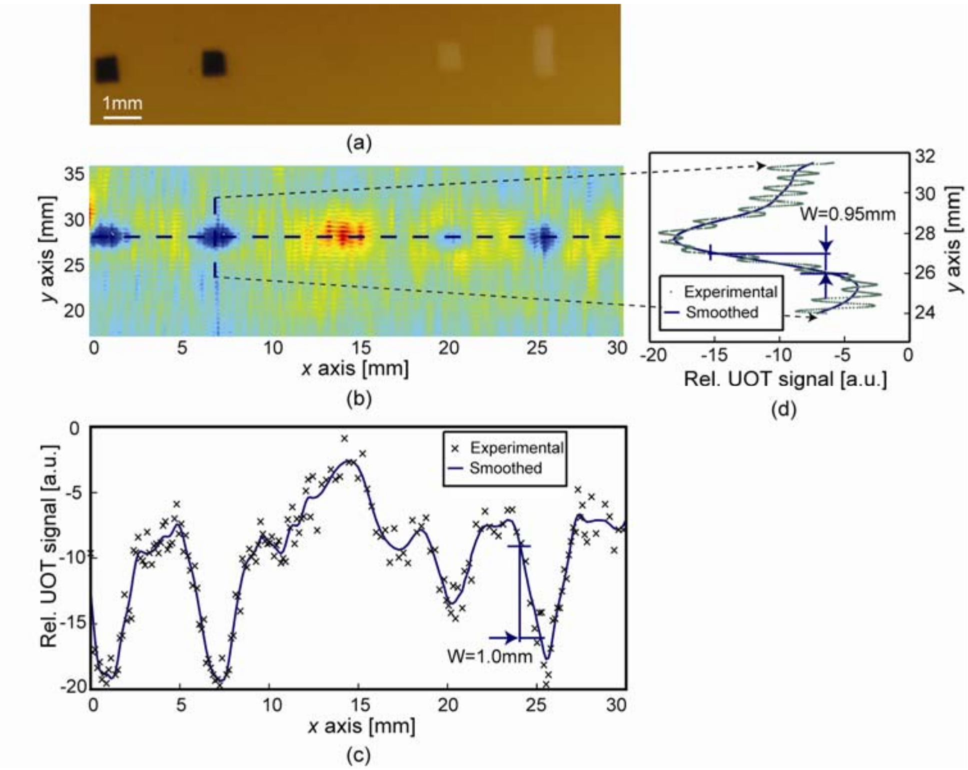

Fig. 3.4. UOT images of the absorbing, scattering, and phase objects embedded in the middle plane of a 30-mm thick intralipid phantom slab. (a) A photograph of the intralipid sample with the five embedded objects: two absorbing objects of dimensions 1.5×1.5×1.5 mm^3 on the left; one phase object of 1.5×1.5×1.5 mm^3 in the middle; two scattering objects of 1.5×1.5×1.5 mm^3 and 2×3×2 mm^3, respectively, on the right. (b) A B-scan image of the five objects obtained from SHB-UOT. (c) A 1D image of the five objects along the B-scan direction, denoted by the horizontal dashed line in (b). (d) An A-scan image of the second absorbing object, denoted by the vertical dashed line in (b). The smoothed curves were obtained by FFT filtering.

A typical imaging result obtained from the UOT experiment with SHB detection is shown in Fig. 3.4, which is a reconstructed image of five objects embedded in a 30-mm thick tissue-mimicking phantom. These objects represent three distinctly different optical heterogeneities commonly encountered in optical imaging of biological tissue: the absorbing objects, the scattering objects, and the phase object—a volume with a uniform refractive index—in a scattering background. The absorbing objects, with the same composition as the background gelatin matrix but dyed with black India ink, have an optical absorption coefficient μ_a = 10 mm^{-1}; the scattering objects, with 3-wt.% intralipid added to the gelatin matrix, have a higher reduced scattering coefficient μ_S' = 3 mm^{-1}; the phase contrast object, made from 10-wt.% gelatin solution that contains no intralipid, is optically transparent and homogeneous. The objects have dimensions of either 1.5×1.5×1.5 mm^3 or 2×3×2 mm^3—much smaller than the ultrasonic focal zone of 16 mm length. Figure 3(a) is a photograph of the sample, dissected at the middle plane, containing all five objects and 3.4(b) is a B-scan UOT image with SHB detection. Figure 3.4(c) shows an A-line image of the second absorbing object, corresponding to the vertical dashed line in 3.4(b). Figure 3.4(d) shows a 1D image of all five objects along the horizontal dashed line in 3.4(b). The imaging results for different objects can be explained by the different mechanisms involved in the ultrasonic modulation of the diffused light[67]. On the one hand, the decrease of the UOT signal at the site of the absorbing objects is due to strong absorption of the diffused photons. On the other hand, the decrease of the signal at the site of higher scattering objects is due to the cancellation of different phase accumulation terms, resulting in a reduction in the amplitude of the ultrasound-modulated light. By contrast, ultrasound-modulated light amplitude is increased at the site of lower scattering/clear objects relative to that of the higher scattering background (e.g., phase objects). It is almost intuitive that the lower the scattering coefficient of the object relative to the background, the stronger the UOT signal[68]. It is therefore feasible, in principle, to map the distribution of the scattering coefficient based on the relative changes in UOT signal. The axial and lateral resolutions of the imaging experiment can be quantified from Fig. 3.4(c) and 3.4(d). The resolution, defined here as the width between the 20% and 80% rise points on either edge of the object, is 0.95 mm along the acoustical axis and 1.0 mm perpendicular to the acoustical axis. The axial resolution is ~60% of the full spatial extent—1.5 mm—of the five-cycle 5 MHz ultrasound burst, indicating good agreement between the experimental measurement and the theoretical expectation. The lateral resolution appears larger than the ultrasonic focal width as a result of the convolution of the ultrasonic focus and the imaging object. This result clearly demonstrates the sensitivity of the technique for imaging all three types of objects of ~millimeter dimensions in the 30-mm deep tissue regime. Especially notable is the improved axial resolution in imaging scattering objects in comparison with the previous study[67], where UOT was first shown to image scattering objects ($2\times2\times20$ mm^3) that occupied the entire length (20 mm) of the ultrasonic focal zone.

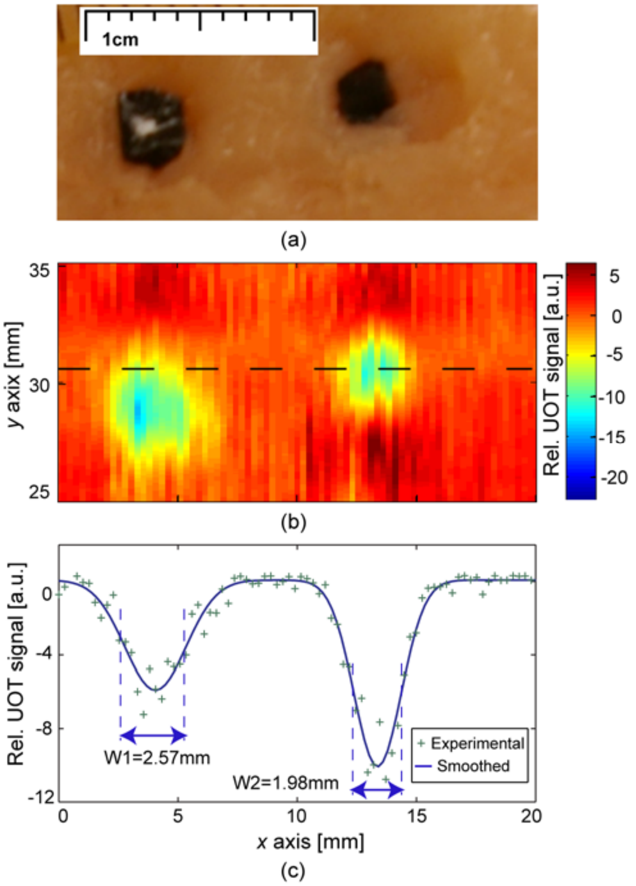

Fig. 3.5. UOT images of a 32-mm thick chicken breast sample. (a) Photograph of the sample embedded with two absorbing objects of absorption coefficient μ_a = 10 mm^{-1} and dimensions $3\times3\times3$ mm^3 and $2\times2\times2$ mm^3, respectively. (b) A B-scan image of the sample. (c) A 1D image of the two objects along the B-scan direction, denoted by the horizontal dashed line (smoothed over the experimental data points) in (b). The smoothed curve was obtained by FFT filtering.

To demonstrate the feasibility of SHB-UOT for deep tissue imaging in real biological samples, a 32-mm thick chicken breast sample was imaged. Two small absorbing objects, made with the same composition as the imaging objects in Fig. 3.4, were embedded 10 mm apart in the middle plane of the sample. The result is shown in Fig. 3.5. The full widths at half maxima of the imaged objects, quantified from Fig. 3.5(c), are 2.6 mm and 2.0 mm, respectively, and agree well with the real dimensions of the objects. The high SNR resulting from the improved SHB detection in UOT makes a prominent distinction between the absorbing objects and the tissue background, which verifies its potential in biomedical imaging, such as in breast cancer screening.

We also acquired a UOT image of a 40-mm thick tissue-mimicking sample. The sample was prepared by mixing 10-wt.% porcine gelatin (Sigma G2500) and 1-wt.% intralipid (Fresenius Kabi) in distilled water and molding the solution into a slab whose dimensions were 100×100×40 mm^3 with the 40 mm thickness along the light propagation direction. The resulting sample had a reduced scattering coefficient of $\mu_S^{'} = 0.7$ mm^{-1} for λ = 793.38 nm, comparable to that of the human breast. Three absorbing cubes were embedded in the middle plane of the sample, with dimensions of 1×1×1 mm^3, 3×3×3 mm^3, and 5×5×5 mm^3, respectively. Their optical absorption coefficient is $\mu_a = 10$ mm^{-1} because of the addition of black India ink to these volumes.

Figure 3.6 shows a typical imaging result obtained from the SHB-UOT experiment, which is a reconstructed image of the three absorbing objects embedded in the sample after a raster scan (B-scan) of the sample along the *x* axis. At each *x* position, the temporal evolution of the UOT signal along the *y* axis (the ultrasound propagation direction) constitutes an A-scan. The image shows very high contrast between the objects and the background matrix.

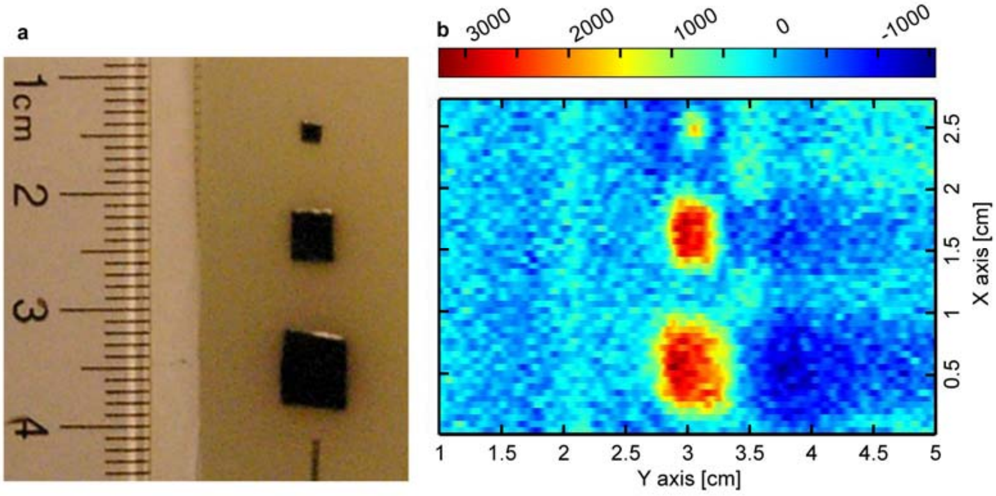

Figure 3.6. UOT image of the three absorbing objects embedded in the middle plane of a 40-mm thick tissue-mimicking phantom. a. A photograph of the sample with the three embedded objects. b. A B-scan image of the three objects obtained from SHB-UOT.

Another interesting feature of SHB detection for UOT is that multiple spectral-holes can be burned and accessed that will transmit multiple sidebands of the ultrasound-modulated light. To demonstrate this, we investigated harmonic imaging using the SHB-UOT system.

The peak to peak pressure at the focus of the 5 MHz ultrasound transducer in the experiment was measured to be 2 MPa. At this magnitude, the nonlinear effect in the ultrasonic waveform is already significant enough that the higher harmonics have come into play in the modulation of the diffused light inside the sample. Fourier analysis shows that the second harmonic frequency of a five-cycle 5 MHz ultrasound burst has a magnitude of 1/3 of its fundamental frequency contribution, as shown in Fig. 3.7a. This implies that in the ultrasound-modulated light, both the 5 MHz and the 10 MHz sidebands exist due to the two frequencies' contribution. When the two AOM's were tuned to burn two spectral-holes at the 5 MHz and 10 MHz sidebands, both components were filtered through the SHB crystal, while the un-modulated light was strongly suppressed. The resulting amplitude of the second harmonic UOT signal was half of the fundamental UOT signal, as shown in Fig. 3.7b, indicting better filtering of the spectral hole for the higher harmonic.

A harmonic imaging result is shown in Figure 3.8. The sample was a 20-mm thick phantom slab having the same composition as the 40-mm thick sample. Two absorbing objects were embedded in the middle plane of the phantom, with dimensions of 5×5×5 mm^3 and 8×8×8 mm^3, respectively. Their optical absorption coefficient is $\mu_a = 10\ \text{mm}^{-1}$ because of the addition of black India ink. Both the fundamental image and the second harmonic image have adequate resolution and contrast to resolve the two absorbing inclusions.

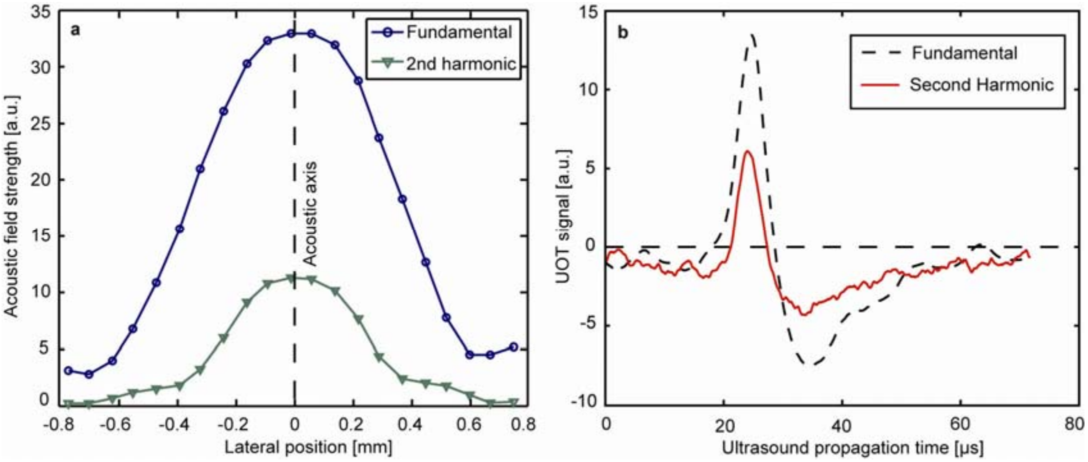

Figure 3.7a. Acoustic pressure contributed by the fundamental and second harmonic frequencies of the 5 MHz focused transducer at its focus perpendicular to the ultrasound propagation direction. 3.7b. The detected UOT signals when a spectral-hole was burned at the fundamental or second harmonic frequency. The ultrasound burst consists of five cycles of a 5 MHz sinusoidal wave emitted by the ultrasound transducer, whose focal pressure is 2 MPa.

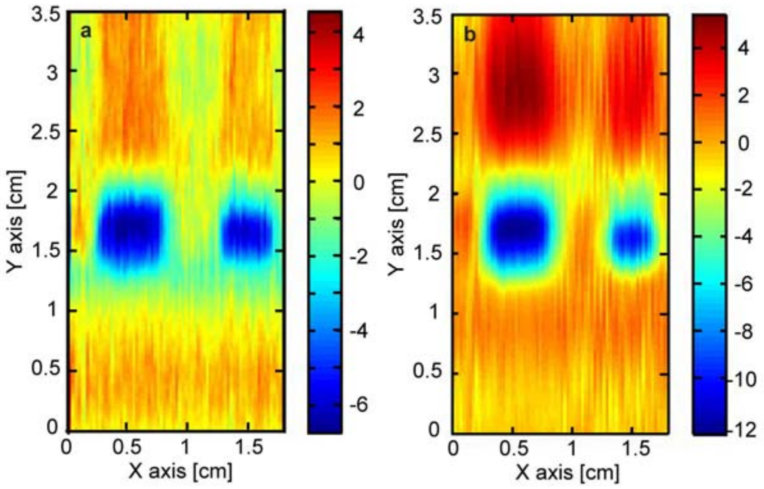

Figure 3.8. Harmonic image of two absorbing objects embedded in a 20-mm thick phantom sample. a. acquired when spectral-holes were burned at the fundamental frequency; b. acquired when spectral-holes were burned at the second harmonic frequency.

3.4 Conclusions

In summary, the SHB-UOT's high resolution and deep imaging ability in biological tissue was experimentally demonstrated. Its ability to distinguish both optically scattering and absorbing heterogeneities from the background tissue was verified. Currently the burned spectral hole is far from saturation because of the limited optical pump power available from the laser. Also, the finite size of the optical window of cryostat limits the achievable etendue in detection of the diffused light. Our double-pass experiment results suggest that by increasing the optical pump power and optical window size of the cryostat, further improvements can be made to exploit the full potential of the SHB detection for UOT. With these improvements, SHB-UOT will be useful for small animal imaging and clinical diagnostic imaging.

The signal detection enhancement by SHB for UOT, as shown in the experimental results, is very encouraging. The most recent SHB-UOT experiment result reported by other groups[69] demonstrated an unprecedented imaging depth of 9 cm in tissue-mimicking phantom samples, which is close to practical applications, such as early breast cancer detection. However, there is still a lot of room to improve this emerging technology. Much improvement has to come from the development of a better SHB material: it needs to have a very high suppression to the un-modulated component, it needs to operate at a optical wavelength within the optical imaging window, it needs to have a longer spectral hole life time, and preferably it can work at higher temperature.

Chapter 4

Time-Reversed Ultrasonically Encoded Optical Focusing

4.1 Motivations

Manipulating light propagation has always been a subject of intense research[33-35, 70-72]. The motivations are obvious: as the only electromagnetic wave sensitive to molecular conformation, light is an essential tool to probe the structure and properties of matter, and to monitor physical, chemical or biological processes. Light instead of harmful x-rays is an ideal nonionizing radiation for imaging and treating biological tissues, and light is also a basic tool in communication and computing. A better understanding and control of light propagation in matter has both immediate benefits and far reaching impacts—indeed, any advance in this subject can be readily transferred to other fields dealing with wave phenomena[73-75].

Of particular interest is the problem of focusing light into a scattering medium. For example, high-resolution optical imaging relies on precisely focusing light into the medium at desired depths; photodynamic therapy and optogenetics require light to be delivered to specific regions of interest inside tissue. However, multiple scattering imposes a fundamental optical diffusion limit on direct light focusing in turbid media. Consequently, the imaging depth of all forms of focusing optical microscopy, such as confocal microscopy, is limited to less than one transport mean free path. A number of technologies have been developed to address this problem. For example, light can be focused through biological tissue by optical phase conjugation[33], or focused into a static scattering medium by iterative wave front shaping that maximizes the signal strength of a blurred yet visible implanted target[35]. However, it is desirable to focus light into (instead of through) a scattering medium, to tolerate dynamic microstructures, and to rapidly adjust the focal position. These challenges have not been met by previous research endeavors. Our method shows great promise in filling this gap.

4.2 Working Principle and Experimental Implementation

Our technique, called Time-Reversed Ultrasonically Encoded (TRUE) optical focusing, combines ultrasonic modulation of diffused coherent light[25, 76] with optical phase conjugation[47, 77-79] to achieve dynamic focusing of light into a scattering medium.

4.2.1 Experimental Set-up

As shown in Fig. 4.1, the light from a laser source (λ = 532 nm) with long coherence length was split into three parts, a sample beam S and two mutually conjugated reference beams R and R^*. S was transmitted through two acousto-optic modulators (AOM) in series to tune its optical frequency to $f_S = f_0 - f_a$ before propagating diffusively through the medium, where f_0 was the laser frequency and f_a was the frequency shift due to the two AOMs. A focused ultrasonic wave of the same frequency f_a traversed the medium and modulated the diffused light. The ultrasonically modulated light could be regarded as emanating from a virtual source that was defined by the ultrasonic focus and was frequency shifted by $\pm f_a$, resulting in two sidebands $S(f_\pm)$ with frequencies $f_+ = f_0$ and $f\_ = f_0 - 2f_a$. This virtual source served as the internal "guide star"[70]. Outside the medium, the diffused light was holographically recorded by a phase-conjugate mirror, here a photorefractive $Bi_{12}SiO_{20}$ (BSO) crystal. The only stationary hologram that could be recorded was from the interference between R and $S(f_+)$[45, 46, 51, 80]. Then, the hologram was read by R^* to generate a time-reversed (TR) copy of $S(f_+)$, denoted as $S^*(f_+)$. By reversibility, $S^*(f_+)$ back-traced the trajectory of $S(f_+)$ and converged to its virtual source, thereby achieving optical focusing into the scattering medium. The energy in $S^*(f_+)$ did not exceed that in $S(f_+)$ as the hologram was read without fixing. However, an intensity gain can be achieved with a higher-intensity shorter-duration readout beam R^*. Further, an energy gain much greater than unity is attainable with hologram fixing or two-step recording[45, 46].

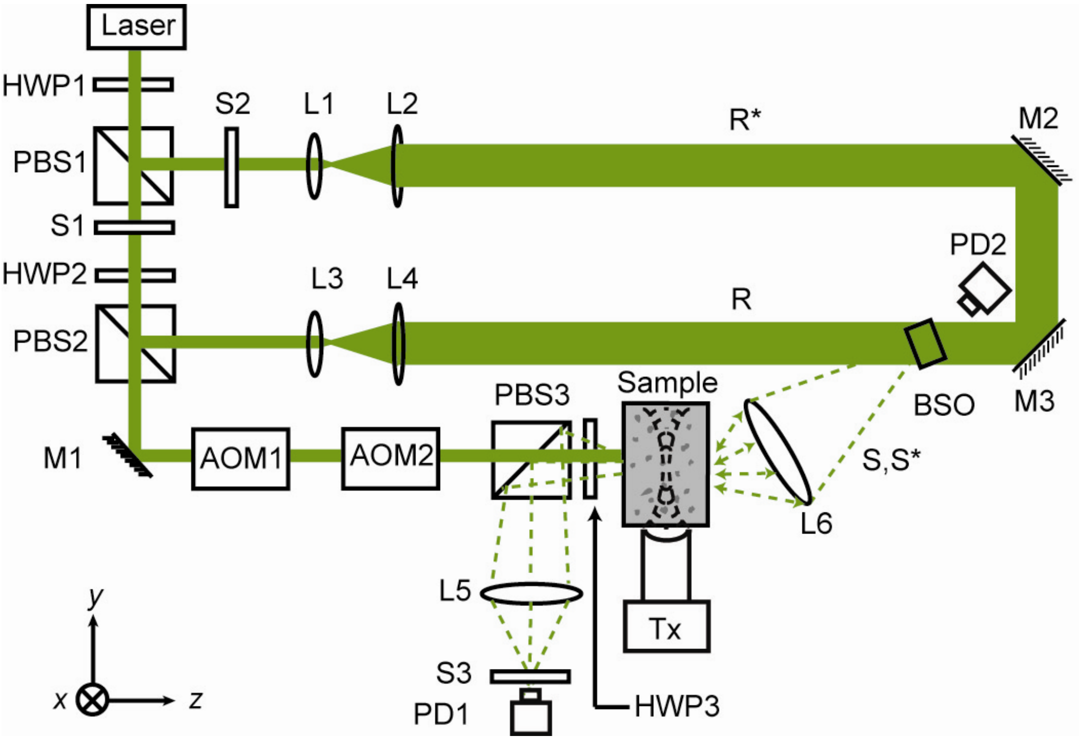

Fig. 4.1. Schematic of the experimental setup for TRUE optical focusing. HWP*i*, *i*th half-wave plate; PBS*i*, *i*th polarizing beam splitter; S*i*, *i*th shutter; M*i*, *i*th mirror; AOM*i*, *i*th acousto-optic modulator; L*i*, *i*th lens; PD*i*, *i*th photodiode; R, reference beam; R*, conjugated reference beam; S, signal light; S*, time-reversed signal light; BSO, $Bi_{12}SiO_{20}$; Tx, ultrasonic transducer with centre frequency f_a = 3.5 MHz, focal length = 38 mm, and focal width = 0.87 mm. Coordinates: x = sample scanning axis, y = acoustical axis, and z = optical axis. The time-reversal procedure consisted of recording and readout of a hologram. To record a hologram, S1 was opened, and S2 and S3 were closed for 190 ms; to read the hologram, S1 was closed, and S2 and S3 were opened for 10 ms.

4.2.2 Monte Carlo Simulation

To illustrate the concept of TRUE optical focusing in a scattering medium, we used a Monte Carlo model[81] to simulate the propagation of the sample light $S(f_S)$ and the ultrasonically encoded $S(f_+)$. The light–medium interaction, dominated by elastic scattering, is characterized by the scattering mean free path L_S and scattering anisotropy g. For example, $L_S \approx 0.1$ mm and g ≈ 0.9 in the human breast[82]. Optical absorption is much weaker than scattering in typical biological tissue and was neglected here. At depths beyond one transport mean free path $L_S' = L_S/(1\text{-g})$, light propagation is sufficiently randomized. In our simulation, a photon was scattered ~ 70 times on average before exiting a scattering layer of thickness $L = 40L_S$. With increasing optical thickness, the intensity of the multiply-scattered light decreases much more slowly than the the intensity of the ballistic light, consistent with our experimental observation. The light that can be holographically recorded and time-reversed is therefore predominantly multiply-scattered.

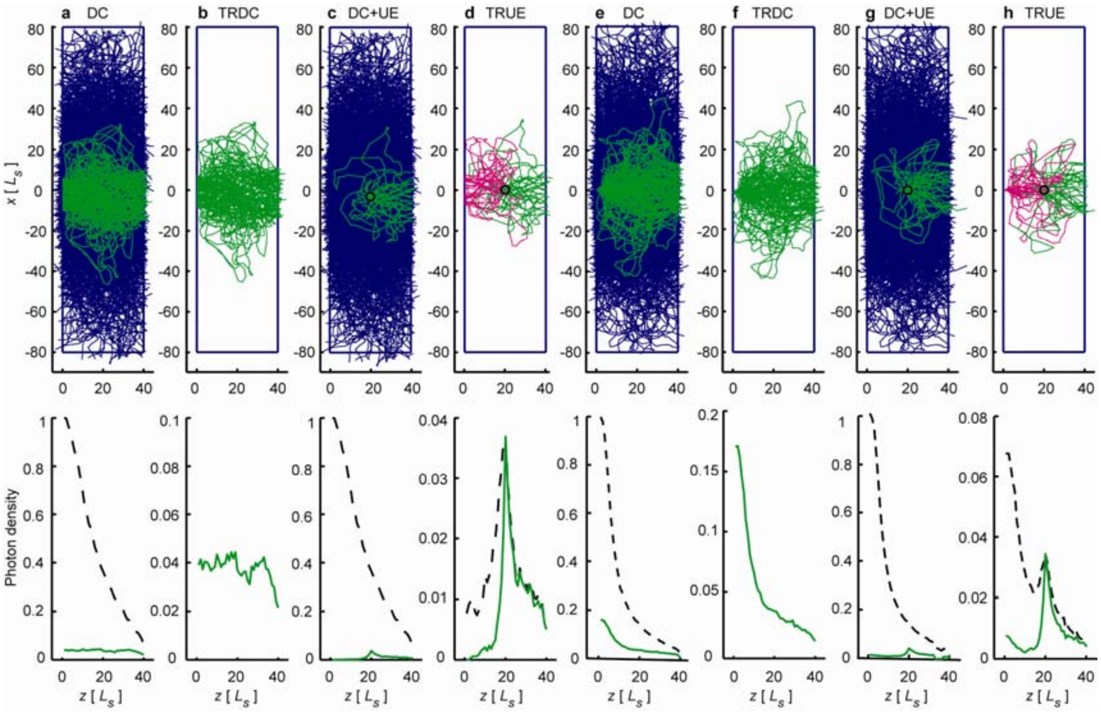

Fig. 4.2. 2D Monte Carlo simulation of light propagation inside a scattering slab whose dimensions were x = $160L_S$ and z = $40L_S$. Initially, a broad (a–d) or a narrow (e–h) light beam was normally incident at the origin of the coordinates. In each panel, the top plot shows the trajectories, while the bottom plot shows the photon density distribution(s) along the optical axis (total density shown in black). a & e, diffusive trajectories of $S(f_S)$ propagating through the slab: some (shown in green) reach the phase-conjugate mirror and the others (shown in blue) do not. b & f, trajectories of $S^*(f_S)$ propagating back through the slab and converging to the incident point. c & g, trajectories of $S(f_S)$ (shown in blue) and the ultrasonically encoded component $S(f_+)$ (shown in green) inside the slab. d & h, trajectories of $S^*(f_+)$ converging back to the ultrasonic focus (shown in green) then back to the incident point (shown in magenta). The black circles in the middle of the slab denote the ultrasonic focus. UE: Ultrasonically Encoded light.

The trajectories of $S(f_S)$, $S(f_+)$, $S^*(f_S)$ and $S^*(f_+)$, shown in Fig. 4.2, appear to be random walks. However, in ideal time reversal, $S^*(f_S)$ and $S^*(f_+)$ would trace back the trajectories of $S(f_S)$ and $S(f_+)$ owing to the deterministic nature of the medium at any instant, leading to the convergence to their sources. Without ultrasonic encoding, $S^*(f_S)$ converged to the incident location of $S(f_S)$. With ultrasonic encoding, $S^*(f_+)$ converged to the ultrasonic focus instead, which is the source of $S(f_+)$.

4.2.3 Experimental Validation

The TRUE optical focusing was validated with imaging experiments (Fig. 4.3). The imaging sample was a 10-mm thick scattering slab, made from a mixture of porcine gelatin, distilled water, and 0.25% Intralipid, resulting in $L_S \approx 0.4$ mm, g ≈ 0.9, and an absorption length $L_a \approx 79$ mm. The light beam started with a 2-mm diameter on the incident plane of the sample and diffused to ~4 mm (FWHM) in the middle plane. The middle plane contained three objects with different compositions: two dyed with black ink (Obj1 and Obj2) and having an optical absorption coefficient $\mu_a \approx 0.8$ mm^{-1}, and one having 1%-concentration Intralipid (Obj3), resulting in an $L_S \approx 0.1$ mm. When the sample was laterally scanned along the x axis, four 1D images were acquired (Fig. 4.3b and 4.3c). The first two were acquired without either AOM tuning or ultrasonic modulation. To form the first image—a "DC" image, $S(f_S)$ was detected by a photodiode at the BSO position. To form the second image—a "TRDC" image, $S^*(f_S)$ was transmitted back through the sample and detected by a photodiode PD1. To form the third image—a "UOT" image based on conventional Ultrasound-modulated Optical Tomography (UOT)[51, 53, 80, 83], $S(f_+)$ was spectrally filtered by the BSO and was then detected by PD2. To form the fourth image—a "TRUE" image, $S^*(f_+)$ was transmitted back through the sample and detected by PD1.

The salient differences in the apparent image resolution and contrast among the four imaging methods stem from the inherently distinct imaging mechanisms. The DC and TRDC imaging methods, suffering from optical diffusion, lacked sufficient spatial resolution to resolve the three objects. The optical diffusion, approximated as a Gaussian profile, was convolved with the object profile to fit the experimental data (see Appendix B for derivation). The full widths at half maxima (FWHM) of the Gaussian profiles, defined as the image resolutions, were 3.4 mm for DC imaging and 3.2 mm for TRDC imaging. By contrast, the UOT and TRUE imaging methods, based on imaging signals emanating from the internal virtual sources, both adequately depicted the profiles of the objects. The ultrasonic focus, approximated as a Gaussian profile, was convolved with the object profile to fit the data. The resolutions were 0.89 mm and 0.63 mm for UOT and TRUE imaging, respectively.

A square law exists if $S^*(f_+)$ indeed converges to the ultrasonic focus: the TRUE signal is proportional to the square of the UOT signal. On the one hand, the optical field for the UOT image $S(x, f_+)|_{\mathrm{BSO}} \propto C(x) \cdot S_{in}(f_S)$, where $C(x)$ is a virtual source term and $S_{in}(f_S)$ is the incident optical field. On the other hand, for the TRUE image, $S^*(x, f_+)|_{\mathrm{BSO}} \propto S(x, f_+)|_{\mathrm{BSO}}$. As $S^*(f_+)$ inversely traverses the sample, the virtual source term in its conjugated form $C^*(x)$ operates on $S^*(x, f_+)|_{\mathrm{BSO}}$. As a result, the optical field detected by PD1 is $S^*(x, f_+)|_{\mathrm{PD1}} \propto C^*(x) \cdot S^*(x, f_+)|_{\mathrm{BSO}} \propto |C(x)|^2 \cdot S_{in}(f_S)$. Therefore, the detected light intensities in

UOT and TRUE imaging are related by $|\, S^*(x, f_+)|_{\mathrm{PD1}}|^2 \propto |S(x, f_+)|_{\mathrm{BSO}}|^4$. This prediction was verified by the normalized amplitudes of the UOT and TRUE images in Fig. 4.3c. Furthermore, if the point-spread functions in UOT and TRUE imaging follow Gaussian profiles, their widths—defining the spatial resolutions—have a √2:1 ratio. This second prediction agrees with the ratio of 1.4 between the image resolutions of UOT (0.89 mm) and TRUE (0.63 mm) imaging. In addition, the resolution of UOT is in agreement with the ultrasonic focal diameter of 0.87 mm.

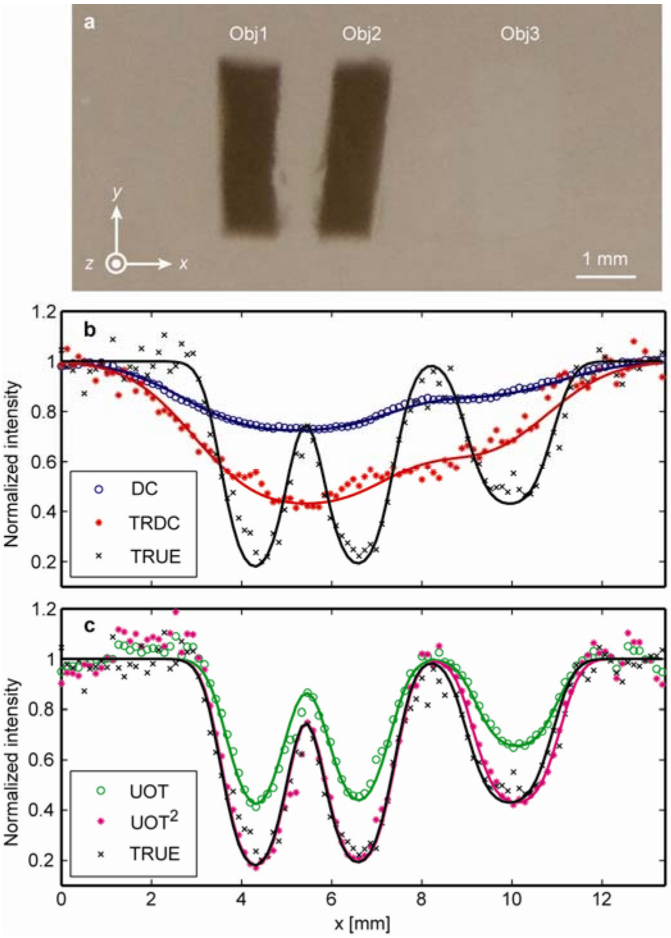

Fig. 4.3. Results from four imaging experiments validating TRUE optical focusing. a, photograph of the imaged sample dissected at the middle plane containing two absorbing objects (Obj1 and Obj2) and one scattering object (Obj3). The object dimensions were x = 1.3 mm, y = 4.5 mm, and z = 1 mm for the two absorbing objects

and x = 1.7 mm, y = 4.5 mm, and z = 0.6 mm for the scattering object, while the full dimensions of the sample were $x = y$ = 60 mm and z = 10 mm. b, comparison of the normalized DC, TRDC, and TRUE images of the sample. The absolute strengths of the TRDC and TRUE signals were ~3,000 mV and ~30 mV, respectively. The objects can not be distinguished in the DC and TRDC images, while in the TRUE image the objects are clearly shown against the background, with 61% contrast for the absorbing objects and 31% contrast for the scattering object. c, comparison of the UOT and TRUE images of the sample to demonstrate the square law: the TRUE signal is proportional to the square of the UOT signal (UOT^2). The FWHMs of the point-spread functions were 0.89 mm (UOT) and 0.63 mm (TRUE), whose ratio is 1.4 ($\approx\sqrt{2}$). In b and c, the symbols represent experimental data, while the solid curves represent Gaussian fitting.

4.2.4 Comparison of TRUE signal to ballistic light

Compared with wavefront correction techniques that require seconds or even minutes, a PRC has much faster response, which monotonically decreases as a function of optical illumination intensity[45] for the formation of a stable hologram. The response time was on the order of 100 ms in our experiment, limited by the weak intensity of the modulated light. During the measurements, the recording time was set to 190 ms, which effectively averaged out influences from ambient sources, e.g., air disturbance. In the reading procedure, the hologram written on the BSO crystal was almost instantly erased by intense illumination, and simultaneously a phase conjugate copy was generated from the diffraction on the crystal. An example of the obtained TRUE signal waveform is shown in Fig. 4.4, and the amplitude of the peak immediately after both shutters S_1 and S_2 are turned on at time 0 is recorded as a TRUE signal. The noise mainly came from shot noise and the spatial noise of randomly distributed charge carriers, both of which can be reduced by coherent averaging.

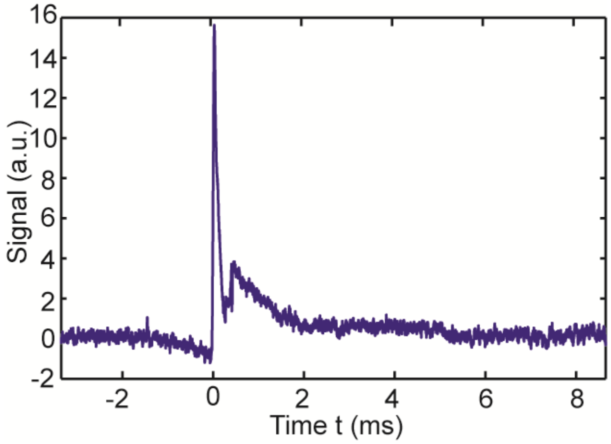

Fig. 4.4. An example waveform of the detected TRUE signal from a 5-mm thick scattering sample with scattering coefficient μ_S = 10 mm^{-1} and scattering anisotropy g = 0.9.

Compared with the exponential decay of ballistic light, the TRUE signal originating from modulated diffused light had a much slower decay rate. Hence, the TRUE signal was more resistant to multiple scattering, and more efficient in delivering energy to a target in biological tissue. After transmission through a turbid layer with an optical thickness of $\mu_t L$, the output ballistic light intensity $I_1 = I_0 \exp(-\mu_t L)$, where I_0 is the input laser intensity, $\mu_t = \mu_S + \mu_a \approx 10$ mm^{-1} is the extinction coefficient, and L is the thickness of the turbid layer. In contrast, the fluence rate of diffused light is characterized by $\exp(-\mu_{eff} D)$, where $\mu_{eff} = \sqrt{3\mu_a (\mu_a + \mu_S')}$ is the effective attenuation coefficient, $\mu_S' = \mu_S (1 - g)$ the reduced scattering coefficient, g the anisotropic factor of a scattering medium, and D the distance between the observation point and the source point[30]. The fluence rate at the middle plane of a diffuse layer, in which the ultrasonic focus modulates the diffused light, is proportional to $\exp(-\mu_{eff} L/2)$. The modulated light is multiply scattered, and the diffusion of modulated light can be again described by diffusion theory, which leads to another decay factor of $\exp(-\mu_{eff} L/2)$. Finally, the fluence rate of the transmitted modulated light is proportional to $\exp(-\mu_{eff} L)$. In the time-reversal phase of TRUE optical focusing, the optical absorption from the medium surface to the virtual source, followed by the random scattering from the virtual source to the opposite tissue surface, further attenuates the TRUE signal. The experimentally measured TRUE signal has a decay rate of 0.32 mm^{-1}, which is greater than $\mu_{eff} = 0.20$ mm^{-1}, as demonstrated in Fig. 4.5.

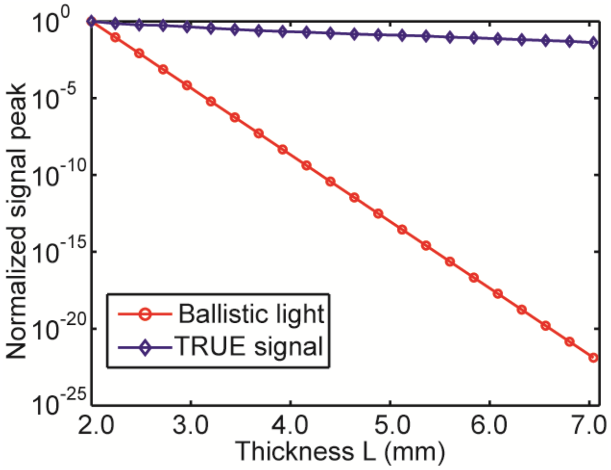

Fig. 4.5. Comparison of the experimental TRUE optical signal and the computed ballistic light signal at different thicknesses *L*. The TRUE signal had a much smaller decay rate, while ballistic light decayed as a negative exponential function of thickness.

4.3 Improving Optical Thickness in TRUE Focusing

In the previous section, we proposed and experimentally validated TRUE optical focusing through a tissue-mimicking phantom sample with an optical thickness of 25. In this section, we report an experimental improvement that resulted in TRUE focusing through turbid media of greater thicknesses[84]. This improvement corresponds to an increase of optical thickness from 37.5 to 70 for the tissue-mimicking phantoms. We also demonstrate the scalability of TRUE focusing with the ultrasonic focus.

4.3.1 Improved Experimental Set-up

TRUE focusing consists of two consecutive procedures, holographic recording and reading. In the recording procedure, light diffuses inside a scattering medium, where part of the light is encoded by a focused ultrasonic wave. The encoded light from this virtual source, noted as S, interferes with a reference beam to form a stable hologram, which is recorded in the photorefractive crystal (PRC). In the reading procedure, both S and R are blocked, and a conjugate reference beam R^*, propagating opposite to R, illuminates the PRC to generate a wavefront S^*, which is the phase conjugate of S. S^* traces back the trajectories of S to the focused ultrasonic region.

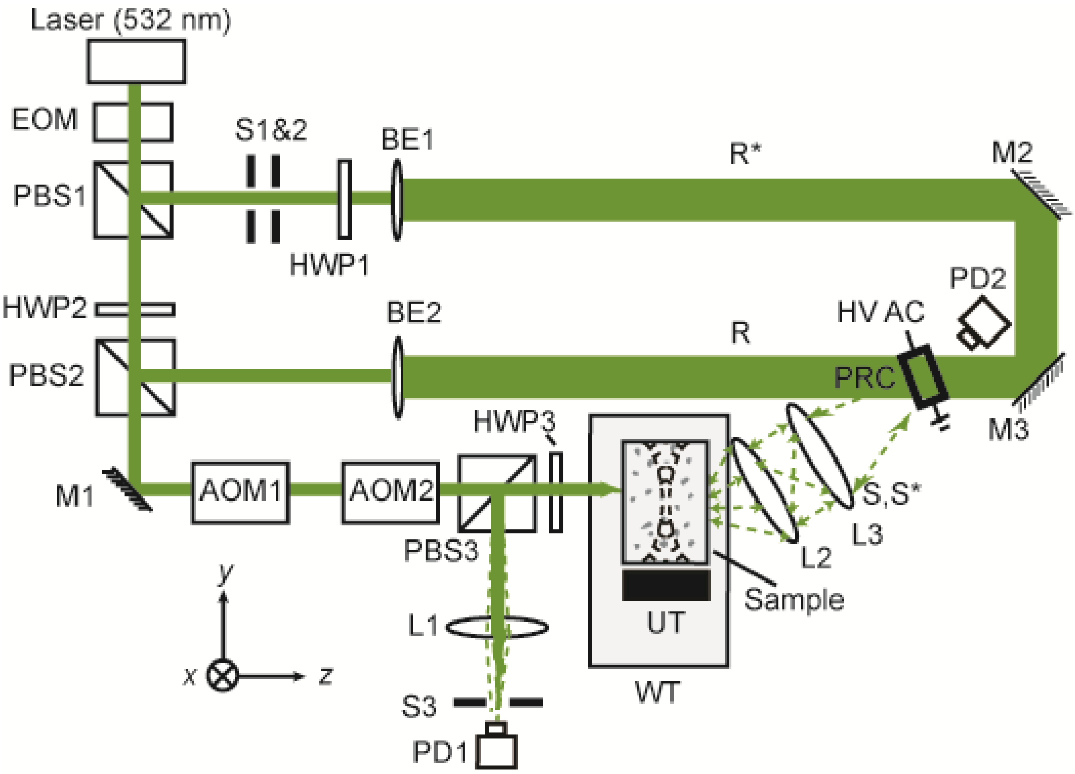
Laser (532 nm)
EOM
S1&2
BE1
R*
M2
PBS1
HWP1
PD2
HWP2
BE2
HV AC
R
PBS2
PRC
HWP3
M3
M1
AOM1
AOM2
S,S*
PBS3
L3
L2
y
Sample
L1
UT
x
z
S3
WT
PD1

Fig. 4.6. Schematic of the improved experimental setup for TRUE optical focusing. EOM, electro-optic modulator; PBS$_{1\text{-}3}$, polarizing beam splitter; S$_{1\text{-}3}$, shutter; HWP$_{1\text{-}3}$, half-wave plate; M$_{1\text{-}3}$, mirror; AOM$_{1\text{-}2}$, acousto-optic modulator; L$_{1\text{-}3}$, lens; PD$_{1,2}$, photodiode; BE$_{1,2}$, beam expander; R, reference beam; R^*, conjugate reference beam;

WT, water tank filled with de-ionized water; UT, ultrasonic transducer; *S*, collected diffused signal light through the sample; S^*, time-reversed signal light; PRC, photorefractive crystal (a 10×10×5 mm^3 BSO was used in the study); HV AC, high voltage AC electrical field; xyz, system coordinates (x = sample scanning axis, y = acoustic axis, and z = axis of incident signal beam propagation).

Figure 4.6 is a diagram of the updated experimental setup for TRUE focusing. A CW diode-pumped solid state laser (Coherent Verdi V-5, λ = 532 nm) was used as the light source. The 45° linearly polarized output from an optical isolator was transmitted through an electro-optic modulator (EOM, Conoptics M350-50) to switch the polarization between the horizontal and vertical states by varying the driving voltage of the EOM. In the recording stage, light was vertically polarized by the EOM, so that almost all of the light was transmitted through PBS1. Then the light was split into a signal beam *S* (with vertical polarization) and a reference beam *R* (also called a pump beam, with horizontal polarization) by a variable beam splitter composed of a half-wave plate (HWP2) and a polarizing beam splitter (PBS2). The signal beam was sent through two acousto-optic modulators AOM1 and AOM2 (IntraAction AOM-802AF1) in series to tune its optical frequency to $f_S = f_0 - f_a$, where f_0 is the laser frequency and f_a is the net frequency shift due to the two AOM's. The signal beam, after passing through PBS3, was incident on the front surface of a tissue-mimicking phantom.

The incident light was multiply scattered in the phantom, and within the focused ultrasonic beam it was encoded by an ultrasonic wave with frequency f_a. Three different ultrasonic transducers were used in the experiment: Panametrics A381S for f_a = 3.5 MHz, Panametrics A302S for f_a = 1 MHz, and Sonic Concepts H-148 for f_a = 2 MHz. A function generator (Agilent 33250A) generated a sinusoidal wave with a specific frequency, amplitude, and burst duration (200 ms), which was synchronized for the whole period of recording and reading. The synchronized wave was sent to a power amplifier (ENI 240L, gain = 50 dB), resulting in focal pressures of 0.70 MPa at f_a = 3.5 MHz, 0.33 MPa at f_a = 1 MHz, and 1.44 MPa at f_a = 2 MHz. The corresponding mechanical indices (MI's) were 0.37, 0.33, and 1.02, respectively. To maximize the ultrasonic encoding efficiency, the ultrasonic focus was aligned to overlap the center of the diffused light profile within the medium. The light encoded by the ultrasonic wave had a frequency shift of f_a.

The transmitted light exiting the back side of the sample consisted of three spectral components: the "un-encoded" photons at $f_S = f_0 - f_a$, and the two "encoded" photons $S(f_+)$ and $S(f\_)$ at $f_+ = f_0$ and $f\_ = f_0 – 2f_a$, respectively. All three light components were collected and mixed with R within a 10×10×5 mm^3 BSO crystal, but only $S(f_+)$ could form a stable interference fringe pattern with R, which was recorded in the crystal; the other frequency components formed traveling interference fringes that were averaged out within the 190 ms recording time. To enhance the recording efficiency, a 2.1 kHz, 8 kV (peak-to-peak) high voltage square wave electrical field was applied across the crystal. The response time of the crystal was approximately inversely proportional to the illuminating light intensity, and was on the order of 100 ms in our study.

In the subsequent reading stage, the EOM changed the laser beam to horizontal polarization. As a result, both the signal and reference beams were now turned off, and the beam reflected by PBS1 formed R^*, which was incident on the crystal in the direction opposite to that of R. The polarization of R^* was tuned by HWP1 to accommodate the optical activity of the BSO crystal. The hologram recorded by S and R in the crystal thus could be read by R^* to generate a time-reversed copy of $S(f_+)$, denoted as $S^*(f_+)$. Due to its reversibility, $S^*(f_+)$ accurately traced back the trajectories of $S(f_+)$ to the focused ultrasonic region, hence achieving optical focusing inside the scattering medium.

In the ultrasonic focal zone, $S^*(f_+)$ was again ultrasonically modulated, resulting in three components: $S^*(f_+)$, $S^*(f_++f_a)$, and $S^*(f_+-f_a)$ (with frequencies at f_0+f_a , f_0+2f_a , and f_0 , respectively). All three components were transmitted through the rest of the sample, with polarization tuned by HWP3 for maximum reflection at PBS3. The time-reversed light was finally focused by lens L1 onto a photodiode PD1 with 13 mm^2 of active aperture (Thorlabs PDA36A). The collected TRUE signal was digitized by an oscilloscope (Tektronix TDS5034) and downloaded to a computer for further processing.

4.3.2 Imaging Results

Three tissue-mimicking phantoms were used in the study. They were made from porcine gelatin, water, and intralipid, with different thicknesses but the same anisotropic factor.

Optical Thickness = 37.5 The first phantom (Fig. 4.7a&b) was 7.5 mm thick, with a scattering coefficient μ_s = 5 mm^{-1} at 532 nm, giving an optical thickness of 37.5. Again, the scattering anisotropy g = 0.9. Two absorption inclusions (Obj 1 and 2) measuring 1.5 × 6.0 × 0.8 mm along their XYZ-axes were embedded in the middle. These inclusions were made of the same material as the background, except that they were dyed with India ink to provide optical absorption contrast (μ_a = 1.17 mm^{-1}). Two ultrasound transducers were used: one with a 3.5 MHz central frequency (Panametrics A381S, focal length F = 38 mm, aperture size D = 19 mm, and focal width w = 0.87 mm) and the other with a 1.0 MHz central frequency (Panametrics A302S, focal length F = 41 mm, aperture size D = 25 mm, and focal width w = 2.49 mm). There exists a relation, $w = cF/f_aD$, where c is the speed of sound in soft tissue. During the experiment, the phantom was scanned along the x axis with respect to the light and ultrasound beams. At each position, both the TRUE signal and the traditional ultrasound-modulated optical tomography (UOT) signal were recorded, from which 1-D TRUE and UOT images were shown as a function of the phantom position (Fig. 4.7c&d). In this study, the laser output was 1.20 W, and the ultrasonic pressures were 0.70 MPa at the 3.5 MHz ultrasonic focus and 0.33 MPa at the 1.0 MHz ultrasonic focus.

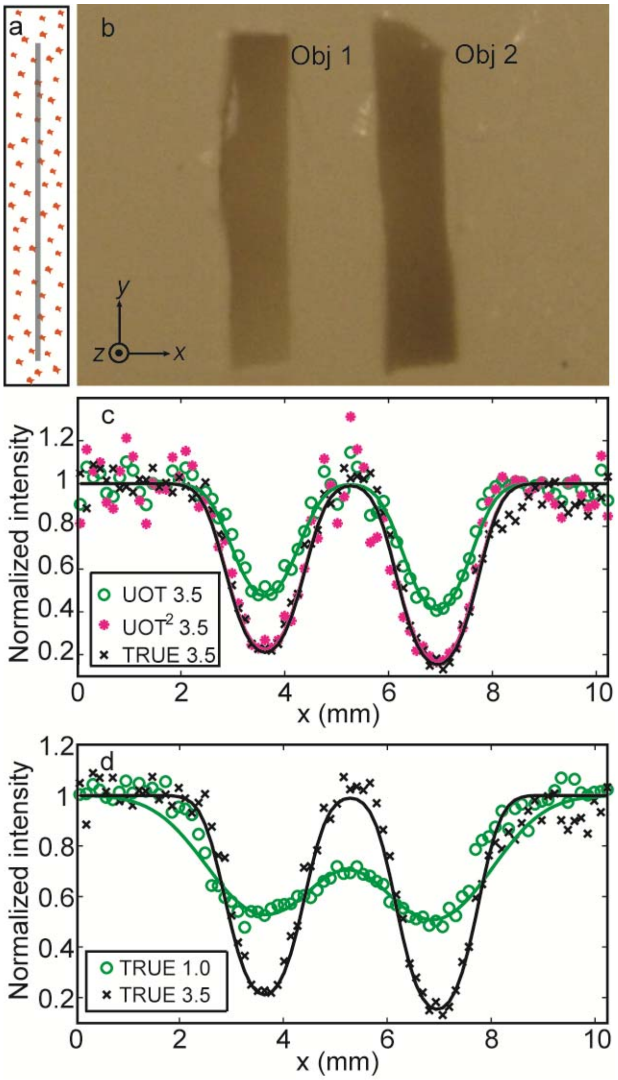

Fig. 4.7. TRUE images of a phantom with an optical thickness of 37.5. a, illustration of the phantom on the YZ plane, showing the plane of the absorbing objects, indicated by the gray line, buried in the middle of the phantom. b, cross-section of the phantom on the central XY plane. The two absorbing inclusions (Obj 1 and Obj 2) had similar dimensions: $x = 1.5$ mm, $y = 6.0$ mm, and $z = 0.8$ mm, while the whole sample's dimensions were $x = y = 60.0$ mm and $z = 7.5$ mm. c, comparison of normalized UOT and TRUE images of the sample with the 3.5 MHz transducer. The fitted TRUE image coincides with the fitted UOT^2 image, which is computed by the mathematic square of the UOT image signal strength. The coefficients of determination R^2 of the TRUE 3.5, UOT 3.5, and UOT^2 3.5 fits are 0.95, 0.93, and 0.90, respectively. Again, the results

verify that the TRUE signal is proportional to the square of the UOT signal (UOT^2), consistent with the square law[85]. d, normalized TRUE images with the 3.5 (black cross) and 1.0 (green circles) MHz transducers. The R^2 value of the 1.0 MHz fit is 0.90. In c and d, the symbols represent experimental data, while the solid curves represent Gaussian fits.

As shown in Fig. 4.7c, both the TRUE and UOT images can distinguish the two objects from the background, and the TRUE image concords with the UOT^2 image. The resolutions of the TRUE and UOT images—defined as the full widths at half maximum (FWHMs) of the approximated Gaussian profiles of the 3.5 MHz transducer—were 0.63 mm and 0.88 mm, respectively. Because of the square law[85], the ratio between the resolutions of the UOT and TRUE images with the same transducer is $\sqrt{2}$. The square relation shows that light can be focused back into a scattering medium with an optical thickness of 37.5, *i.e.*, an equivalent thickness of 3.75 mm in tissue. Fig. 4.7d shows the comparison of the normalized TRUE images obtained with a 3.5 MHz transducer (represented by black crosses and solid line) and with a 1.0 MHz transducer (represented by green circles and line). The spatial (FWHM) resolution of the 1.0 MHz TRUE image was 1.60 mm. The ratio 2.49 mm/1.60 mm equals 1.5, which agrees with $\sqrt{2}$. The poor resolution in the 1.0 MHz image is also accompanied by a low imaging contrast of 16%, defined by $(I_{\max} - I_{\min})/(I_{\max} + I_{\min})$, where I is the relative signal amplitude. In comparison, the 3.5 MHz TRUE measurement achieves an imaging contrast of 73%. Obviously, tighter focusing can be achieved with higher frequency ultrasound. Nevertheless, encoding efficiency is inversely proportional to the square of the ultrasonic frequency. Using the 3.5 MHz transducer working at the optimal output, we found that light could not be focused into a 5 mm thick tissue-mimicking sample with μ_s= 10 mm^{-1}, even when the laser output was raised to 1.80 W.

Optical Thickness = 50 To focus into a thicker scattering sample, in addition to increasing the laser output to 1.80 W, more efficient ultrasonic encoding was applied by using a 2.0 MHz HIFU transducer (Sonic H-148, focal length F = 63 mm, aperture size

D = 64 mm, and focal width w = 0.70 mm). Optimized pressure at the ultrasonic focus was 1.44 MPa. Fig. 4.8 shows the results acquired from a 5 mm-thick phantom, whose scattering coefficient μ_s=10 mm^{-1} and optical thickness was 50, equivalent to a 5 mm thick tissue. Three inclusions—Obj 1 and 2 (absorbing) and Obj 3 (scattering)—were embedded in the middle plane of the phantom, as shown in Fig. 4.8a.

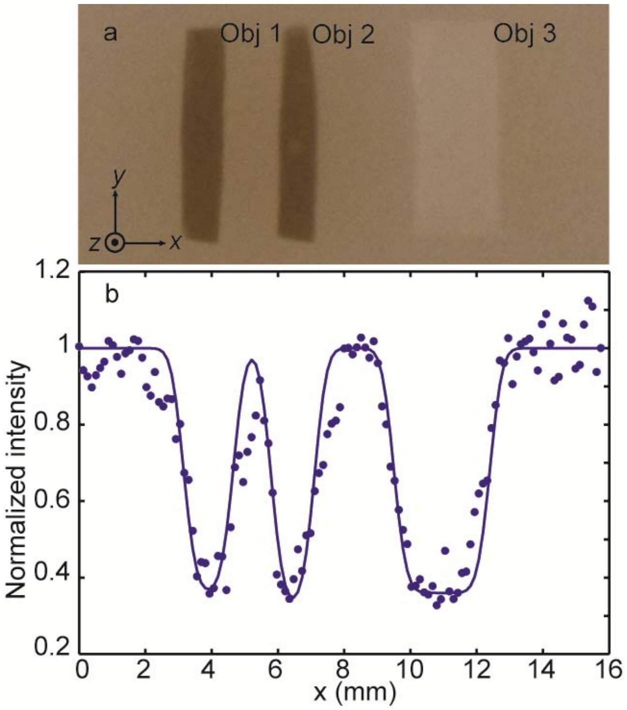

Fig. 4.8. TRUE image of a phantom with an optical thickness of 50 with the 2.0 MHz HIFU transducer. a, photograph of the sample dissected at the middle plane, which contains two absorbing objects (Obj 1 and Obj 2, absorption coefficient μ_a = 0.80 mm^{-1}, scattering coefficient μ_s = 10 mm^{-1} , and scattering anisotropy g = 0.9) and one scattering object (Obj 3, scattering coefficient μ_s = 50 mm^{-1} and scattering anisotropy g = 0.9). The widths of the three objects were 1.4 mm, 1.2 mm and 3.3 mm, respectively, and their lengths and thicknesses were all 6.1 mm and 0.7 mm, respectively. b, normalized TRUE images as a function of phantom position along the x direction.

In Fig. 4.8b, the blue dots (experimental data) and solid line (Gaussian fit) represent the TRUE image with the 2.0 MHz transducer. As we can see, the experimental data and the Gaussian fit agree quite well (R^2=0.90), giving an imaging spatial resolution (FWHM) of 0.50 mm, which equals the value of the 2.0 MHz transducer focal width (0.70 mm) over $\sqrt{2}$. The imaging results verified that light was focused into the tissue-mimicking phantom at a depth of 2.5 mm, and the focus was determined by the focal region of the 2.0 MHz transducer.

Optical Thickness = 70 Based on current setup, the maximum obtained TRUE focusing optical thickness was 70, *i.e.*, equivalent to a 7 mm tissue thickness, and the results are shown in Fig. 4.9. The agreement between experimental data and the fitted curve, despite the relatively low signal-to-noise ratio (SNR) as indicated by an R^2 of 0.86, demonstrated that light was indeed focused to the ultrasonic focus within the 7 mm thick tissue-mimicking sample.

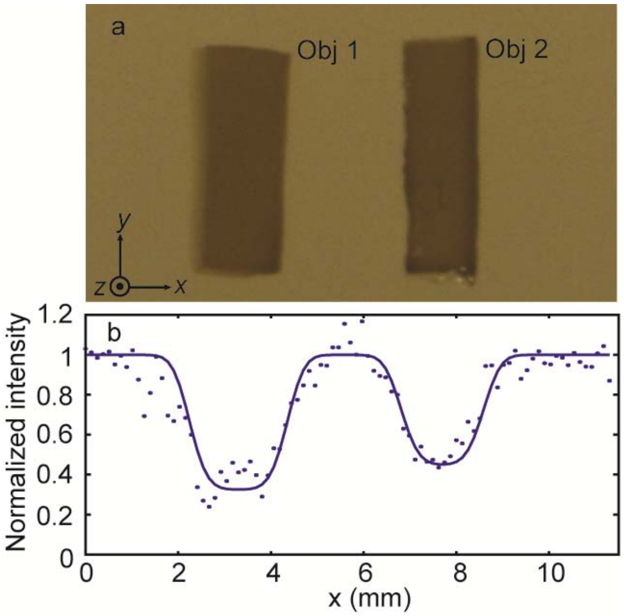

Fig. 4.9. TRUE image of a phantom with an optical thickness of 70 with the 2.0 MHz HIFU transducer. a, photograph of the sample with two absorption objects (Objs 1 & 2) embedded in the middle plane. The widths of the two objects were 2.0 mm and 1.7 mm, respectively, and their lengths and thicknesses were all 6.0 mm and z = 0.7 mm.

The full dimensions of the sample were 60 × 60 × 7 mm^3. b, a TRUE image of the sample.

4.4 Discussion

Previous research endeavors to overcome the depth limitation on optical focusing and light propagation in turbid media include optical clearing, optical phase conjugation (OPC), and adaptive wavefront shaping. Optical clearing alters the optical properties of the medium by introducing optical clearing agents into the medium; OPC can be used for turbidity suppression only through, rather than into, a scattering medium; adaptive wavefront shaping is implemented through a time-consuming feedback loop which relies on the presence of an extraneous guide star. All of these methods lack a mechanism for dynamic, real time light focusing into an arbitrary location inside a scattering medium. In contrast, TRUE optical focusing achieves this goal by first encoding the diffused coherent light with a focused ultrasonic wave which scatters 1000 times less than light in soft biological tissue, and then by optically time reversing only the ultrasonically encoded light.

Focusing into a scattering medium is much more valuable than focusing through it. In practice, the former can be reduced to the latter by moving the focal position. Focusing through a medium is used to image a target only outside a scattering medium, which can be either viewed directly from the target side or scanned by a collimated laser beam. Focusing into the medium must be invoked to image or treat a target embedded inside a scattering medium. For example, when a tumor inside biological tissue is optically imaged or treated, light must be focused to the tumor.

Dynamically focusing light into a scattering medium, with sufficient speed and localization, can profoundly benefit studies involving photophysical, photochemical, and photobiological processes. This work has demonstrated the feasibility of TRUE optical focusing by combining two key mechanisms—localized ultrasonic encoding of the diffused light and selective time reversal of the encoded light—to suppress the scattering effect. The focal spot size can be flexibly scaled with the ultrasonic frequency, and the experimental system can be adapted for reflection or other configurations according to the application. Improvements can be made by using faster photorefractive materials, time-reversal techniques with energy gains greater than unity, and more efficient time-reversal configurations. By delivering light into a small targeted volume deep within a scattering medium, TRUE optical focusing can be used as a universal imaging and light manipulation enhancement method rather than just a specific imaging modality. It has a number of important applications in biomedicine alone, including imaging, sensing, manipulation, and therapy. For deep-tissue imaging and sensing, focusing light improves the spatial resolution and the signal-to-noise ratio. For manipulation, focusing light improves penetration without damaging superficial tissue. For therapy, focusing light enables treating the tumour without harming the surrounding normal tissue. Therefore, TRUE optical focusing can potentially improve applications such as fluorescence tomography, oximetry, optogenetics, nerve stimulation, photodynamic therapy, and photothermal therapy.

Chapter 5

Conclusions

5.1 Summary of Work Done

The work presented in this dissertation can be divided into two parts. The first part focused on improving the signal detection efficiency for a hybrid optical imaging modality, namely ultrasound-modulated optical tomography. The second part focused on developing a method, TRUE optical focusing, that effectively focuses light into scattering media. On the one hand, UOT is just one of the many emerging optical imaging modalities that aim at imaging soft biological tissues; on the other hand, TRUE focusing is developed as a universal imaging enhancement tool. While TRUE optical focusing found its motivation and required expertise for implementation deeply rooted in all of the imaging modalities within our previous research (such as UOT), it is distinctly different from the previous endeavor. Its impact goes far beyond the scope of optical imaging. Because of its potential impact on both imaging and non-imaging applications that require light focusing or delivery deep into scattering media, TRUE optical focusing shall be considered and developed as a universal imaging and light manipulation enhancement method rather than a specific imaging modality.

Two different detection systems in UOT—one based on photorefractive effect and the other on SHB—were explored. Both systems can parallel process multiple speckles of the diffused signal wavefront, resulting in an increased etendue in the signal detection. The SHB crystal-based detection has an added advantage in that it is also immune to speckle decorrelation. Thus, in theory the SHB crystal-based detection is best suited for UOT.

PRC-UOT In contrast to the initial implementation of PRC-based detection for UOT, where pulsed ultrasound was used to modulate the diffused light inside scattering media, we propose a PRC-based UOT system with a quasi-CW ultrasound modulation scheme, where a one-millisecond long focused ultrasound burst was applied to the sample, and the temporal revolution of the detected optical signal was recorded to image both the optical and mechanical properties of the sample. The benefits of using a millisecond long ultrasound burst are twofold: it improves the SNR; and it also enables the detection of the effects of the acoustic radiation force, which happens on the millisecond time scale and can be related to the mechanical properties of the sample. We demonstrated, using this system, that both optical and acoustical heterogeneities could be imaged inside 4-cm thick biological tissue with 2 mm resolutions.

SHB-UOT In the work on SHB-aided detection for UOT, we increased the transmission efficiency of the spectral hole with the available optical intensity, and applied the SHB-UOT system to image thick tissue-mimicking phantom and chicken breast tissue. We demonstrated that absorbing, scattering, and phase objects embedded in the middle plane of a 40-mm thick phantom can be imaged with this system, with a lateral imaging resolution of 0.5 mm and an axial resolution of 1.5 mm as determined by the ultrasound transducer. UOT image was also acquired of a 32-mm thick chicken breast sample embedded with several targets. Further, we demonstrated the feasibility of harmonic imaging in UOT by burning and accessing multiple spectral-holes in a single SHB crystal. The results suggest that the improved SHB-UOT system is one step closer to becoming a practical optical imaging application in biological and clinical studies.

TRUE In the work on TRUE optical focusing, we proposed, experimentally implemented, and validated this novel technique to focus light into scattering media by combining two key mechanisms: localized encoding of the diffused light and selective time reversal of the encoded light. Our experimental system has since been improved to focus light into greater depths. TRUE focusing has been demonstrated on thick scattering media of optical thickness up to 70. With our invention, the chaotic multiple light scattering that deprives optical imaging of spatial resolution in biological tissues is no longer an unbreakable barrier. TRUE focusing opens the door to imaging and treating tissues (e.g., breast tumor) with high precision using harmless light instead of harmful X-ray.

5.2 Directions for Future Work

Biomedical optical imaging is a fast growing field, with many exciting new developments emerging every year. In order to grow into a mature technology and be ready for real life applications such as clinical diagnosis, both UOT and TRUE focusing need further development. Each has to overcome technical barriers along the way.

For UOT, the imaging depth must be enhanced for it to be clinically useful. If UOT can be used to image optical and/or mechanical heterogeneities at depths greater than 100 times its imaging resolution, e.g., at 5 cm imaging depth with 0.5 mm resolution, then it will become a very powerful diagnostic tool for breast cancer detection. With our PRC-based system, UOT images can be acquired from beneath a 4-cm thick chicken breast tissue with 2 mm imaging resolution. With our SHB-UOT system, images can be acquired from a beneath 3.2-cm thick chicken breast tissue with 0.5 mm imaging resolution. These are very encouraging achievements towards real world application.

For PRC-UOT The 532 nm optical wavelength used is not ideal for biomedical imaging because of the high optical absorption by biological tissue. By switching to another wavelength (e.g., λ = 700 nm) in the NIR, whose optical absorption is one order less in biological tissue, greater imaging depth can be achieved for the PRC-UOT system. Equally important for *in vivo* biomedical imaging application is the fast response time requirement for the PRC's used, which must be faster than the speckle decorrelation imposed by the biological tissue, usually less than 1 ms.

For SHB-UOT Improvements can be made to push the SHB-UOT system toward practical application. Most of these improvements have to come from finding or developing a better SHB material that meets the following requirements: it needs to have a very high suppression to the un-modulated component, it needs to operate at a optical wavelength within the optical imaging window, it needs to have a longer spectral hole life time, and preferably it can work at higher temperature.

For TRUE focusing Just one year after its first successful experimental demonstration, this invention has already shown great promise and opened exciting possibilities in optical imaging, manipulation, and therapy. However, great technical difficulties have to be overcome to deliver the promise. Like the PRC-UOT system, TRUE focusing needs to work at a wavelength which has less absorption in biological tissues, and the PRC's must have a faster response time to accommodate the shorter speckle decorrelation time of *in vivo* biological tissue study. In the current experimental configuration, the time reversal gain, defined as $|S^*(f_+)|^2/|S(f_+)|^2$, is far less than unity because reading a recorded hologram simultaneously erases it. This necessitates an OPC mechanism for "reading without erasure", which is possible with "two-step recording". In this scheme, holographic recording by R and $S(f_+)$ of a longer wavelength is enabled by simultaneously illuminating the photorefractive material with a short-wavelength light which sensitizes the photorefractive material. In the absence of the short-wavelength light, holographic read-out by R^* is non-destructive at the absence of the short-wavelength light. Thus, arbitrary intensity and duration of $S^*(f_+)$ are attainable at the focus.

Appendix A

Two Dimensional Monte Carlo Simulation of Light Propagation inside a Scattering Slab

```
clear all;
close all;

% inputs
Ls = 1;     % scattering mean free path is set as unit length
g = 0.9;    % typical anisotropy for tissue
N_photon = 100; % number of photons to simulate

% preallocate memory for matrix to store photon trajectory
MaxSteps = 500; coordinates = 4;
A = zeros(N_photon, MaxSteps, coordinates); % initialize photon trajectory
R_photon = zeros(N_photon,7);     % initialize photon record array
% R_photon(photon#i,1)= isStop: 1, crossing boundary; 2, trapped inside
% after MaxSteps.
% R_photon(photon#i,2)= # of steps=rp,
% R_photon(photon#i,3)= exit side:-1,left;+1,right;-2,bottom;+2,top.
% R_photon(photon#i,4)= exit uz,
% R_photon(photon#i,5)= exit ux,
% R_photon(photon#i,6)= TR?: 1, can be time reversed; 0, No.
% R_photon(photon#i,7)= TR_UOT?: 1,  yes; 0, no.
```

```
N_trapped = 0; % number of photons trapped inside after MaxSteps
s_ = 0; % random seed

% set boundary
x_bottom = -80*Ls; x_top = 80*Ls;
z_left = 0; z_right = 20*Ls;

% set US focus, assuming it's a circle centered at the middle of the sample
z_us = z_left + 0.5*(z_right-z_left);
x_us = 0;
r_us = 2*Ls; % assuming US focus diameter=4Ls

% set collecting lens parameters, assuming lens dia = 30mm = 75Ls, f ~ 30mm
% assuming the lens is 42mm (125ls) away from the back side of the sample
z_lens = 125*Ls;
x1_lens = -37.5*Ls; x2_lens = 37.5*Ls; % bottom and top edge of the lens
% assuming only light exit from -5mm < x < 5mm can be collected by the lens
x1_collect = -12.5*Ls; x2_collect = 12.5*Ls;
% slopes of the two boundaries that define the field of view of the lens
% relative to the collecting area.
k1 = (x1_lens-x1_collect)/(z_lens-z_right);
k2 = (x2_lens-x2_collect)/(z_lens-z_right);

% set array for the boundary of the scattering medium
for i=1:(z_right-z_left+1)
   p_bottom(i,1) = i - 1 + z_left; p_bottom(i,2) = x_bottom;
   p_top(i,1) = i - 1 + z_left; p_top(i,2) = x_top;
end

for j=1:(x_top-x_bottom+1)
   p_left(j,1) = z_left; p_left(j,2) = j - 1 + x_bottom;
```

```
    p_right(j,1) = z_right; p_right(j,2) = j -1 + x_bottom;
end


figure;
axis equal; axis xy;
xlim([z_left-5*Ls z_right+5*Ls]); ylim([x_bottom-5*Ls x_top+5*Ls]);
hold on;
plot(p_bottom(:,1), p_bottom(:,2), 'LineWidth', 2);
plot(p_top(:,1), p_top(:,2), 'LineWidth', 2);
plot(p_left(:,1), p_left(:,2), 'LineWidth', 2);
plot(p_right(:,1), p_right(:,2), 'LineWidth', 2);
xlabel('z [L_s]'); ylabel('x [L_s]');


for n = 1:N_photon
    rp = 1; % initialize row pointer to first row
    uz = 1; % initialize photon direction
    ux = 0; % initialize photon direction
    x = 0; z = 0; % photon injected at (z0,x0)=(0,0)
    A(n,1,1) = x; A(n,1,2) = z; A(n,1,3) = uz; A(n,1,4) = ux;
    isStop = 0;



    while (isStop==0)
        % move photon
        % generate step size
        if s_ == 0
            s_ = -log(rand);
        end
        s = s_*Ls;
        x = x + ux*s;
        z = z + uz*s;
```

```
rp = rp+1;
s_ = 0;
A(n,rp,1) = z; A(n,rp,2) = x;

% check if crossing boundary
if (x < x_bottom)||(x > x_top)||(z < z_left)||(z > z_right)
   isStop = 1;
   if (z < z_left)
      R_photon(n,3) = -1; % -1 if exit from front side
   else
      if (z > z_right)
         R_photon(n,3) = 1;   % +1 if exit from back side
         % Find out if the photon can be Time Reversed
         % see if the photon is within the FOV of the lens.
         % First check coordinates
         if ((x-x1_collect)>(k1*(z-z_right)))&&((x-x2_collect)<(k2*(z-z_right)))
            % Then check direction
            k_down = (x1_lens-x)/(z_lens-z); k_up = (x2_lens-x)/(z_lens-z);
            if (ux>=uz*k_down)&&(ux<=uz*k_up)
               R_photon(n,6)=1; % the photon can be time reversed.
            end
         end
      else
          if (x < x_bottom)
             R_photon(n,3) = -2; % -2 if exit from bottom
          else
             R_photon(n,3) = 2;  % +2 if exit from top
          end
      end
   end
   % skip to the next iteration of the while loop, where the
```

```
    % condition (isStop==0) won't be satisfied, so the control
    % returns to the next iteration of the for loop.
    continue;
else
    if (rp == MaxSteps)  % check if # of steps reaches maximum
        isStop = 2;
        % skip to the next iteration of the while loop, where the
        % condition (isStop==0) won't be satisfied, so the control
        % returns to the next iteration of the for loop.
        continue;
    end
end
%Calculate scattering angles
if g == 0
    cos_s = 2*rand - 1;
else
    cos_s = 1/(2*g)*(1+g^2-((1-g^2)/(1-g+2*g*rand))^2);
end
%Calculate new direction cosines
sin_s = sign(rand-0.5)*(1 - cos_s^2)^0.5;
if abs(uz) < 0.99999
    ux_p = sin_s*ux*uz/(1-uz^2)^0.5+ux*cos_s;
    uz_p = -(1-uz^2)^0.5*sin_s+uz*cos_s;
else
    ux_p = sin_s;
    uz_p = sign(uz)*cos_s;
end
ux = ux_p;
uz = uz_p;
% update the photon trajectory
A(n,rp,3) = uz; A(n,rp,4) = ux;
```

```
    end
    % when exiting the while loop, these entries need to be updated, even
    % when no scattering occurs between step #(rp-1) and #rp. this is done
    % for completeness of the trajectory.
    A(n,rp,3) = uz; A(n,rp,4) = ux;
    % book keeping photon record
    R_photon(n,1) = isStop; % 1 means exit from boundary, 2 means trapped
    R_photon(n,2) = rp; % # of steps inside, (0,0) is the 1st step
    R_photon(n,4) = uz; R_photon(n,5) = ux;

    if (isStop==1)
        plot(A(n,1:rp,1), A(n,1:rp,2));
    else
        if (isStop==2)
            N_trapped = N_trapped + 1;
        end
    end
end

% plot TR light
figure;
axis equal; axis xy;
xlim([z_left-5*Ls z_right+5*Ls]); ylim([x_bottom-5*Ls x_top+5*Ls]);
hold on;
plot(p_bottom(:,1), p_bottom(:,2), 'LineWidth', 2);
plot(p_top(:,1), p_top(:,2), 'LineWidth', 2);
plot(p_left(:,1), p_left(:,2), 'LineWidth', 2);
plot(p_right(:,1), p_right(:,2), 'LineWidth', 2);
xlabel('z [L_s]'); ylabel('x [L_s]');
for n = 1:N_photon
    if R_photon(n,6)==1
```

```
        plot(A(n,1:R_photon(n,2),1), A(n,1:R_photon(n,2),2), 'g');
    end
end

% find out if which photons qualify for TR_UOT
for n = 1:N_photon
    if R_photon(n,6)==1 % must first qualify for TR
        % make a copy of the current photon trajectory to B.
        N_steps = R_photon(n,2);
        B = squeeze(A(n,1:N_steps,:));
        % check if the photon trajectory pass through the US focus O
        % this is done in the following procedure
        % first, for all paths r(j,j+1), find out if the distance OD from
        % the US focus (z_us,x_us) to r(j,j+1) satisfes OD < r_us.
        % If this is true, then find out if the perpendicular foot D is
        % inside the section r(j,j+1).
        % Assuming (z1,x1) is the coordinates of the point r(j), (z0,x0)
        % is the coordinates of the US focus O, (uz,ux)=(kz,kx) is the
        % direction of r(j,j+1), and (zd,xd) the coordinates of D, then:
        % zd = ux^2*z1+uz^2*z0+uz*ux*(x0-x1);
        % xd = ux^2*x0+uz^2*x1+uz*ux*(z0-z1);
        % |OD| = |ux*(z1-z0)+uz(x0-x1)|;
        for j = 1:N_steps-1
            z1=B(j,1); x1=B(j,2); uz=B(j,3); ux=B(j,4);
            OD = abs(ux*(z1-z_us)+uz*(x_us-x1));
            if OD<=r_us
                zd = ux^2*z1+uz^2*z_us+uz*ux*(x_us-x1);
                xd = ux^2*x_us+uz^2*x1+uz*ux*(z_us-z1);
                if (zd-z1)*(B(j+1,1)-zd)>0
                    R_photon(n,7) = 1;
                    % if a photon is found to cross US at step (j,j+1) then
                % there is no need to track the remaining steps. go to
                % the next photon
                break;
            else
                if zd == z1 % in case r(j),r(j+1)and D has same z.
                    if (xd-x1)*(B(j+1,2)-xd)>0
                        R_photon(n,7) = 1;
                % if a photon is found to cross US at step (j,j+1) then
                % there is no need to track the remaining steps. go to
                % the next photon
                        break;
                    end
                end
            end
        end
    end
end
end

% plot TR_UOT light
figure;
axis equal; axis xy;
xlim([z_left-5*Ls z_right+5*Ls]); ylim([x_bottom-5*Ls x_top+5*Ls]);
hold on;
plot(p_bottom(:,1), p_bottom(:,2), 'LineWidth', 2);
plot(p_top(:,1), p_top(:,2), 'LineWidth', 2);
plot(p_left(:,1), p_left(:,2), 'LineWidth', 2);
plot(p_right(:,1), p_right(:,2), 'LineWidth', 2);
xlabel('z [L_s]'); ylabel('x [L_s]');
for n = 1:N_photon
    if R_photon(n,7)==1
```

```
        plot(A(n,1:R_photon(n,2),1), A(n,1:R_photon(n,2),2), 'r');
    end
end
```

Appendix B

Derivation of the Image Resolution in TRUE Optical Imaging Experiment

Below is a brief derivation of the image resolution for the TRUE optical imaging experiment.

In DC and TRDC imaging, the optical diffusion profile at the middle plane of the scattering layer can be approximated as a Gaussian profile g(x), while the embedded object profile can be approximated as f(x). By contrast, in UOT and TRUE imaging, the ultrasonic focus can be approximated as a Gaussian profile g(x), while the embedded object profile is still expressed as f(x).

$$g(x)=\frac{1}{\sqrt{2\pi}\sigma}\exp\left(-\frac{x^2}{2\sigma^2}\right),\ f(x)=\begin{cases}A, & -\frac{L}{2}\le x\le\frac{L}{2}\\ 0, & \text{otherwise}\end{cases}$$

$$g(x)=\frac{1}{\sqrt{2\pi}\sigma}\exp\left(-\frac{x^2}{2\sigma^2}\right)\text{or } X\sim N\left(0,\sigma^2\right)\rightarrow g(z)=\frac{1}{\sqrt{2\pi}}\exp\left(-\frac{z^2}{2}\right)\text{or } Z\sim N(0,1),\ z=\frac{x}{\sigma}.$$

The convolution of g(x) and f(x) yields the imaging resolution.

$$f * g(x) = \int_{-L/2}^{L/2} \frac{A}{\sqrt{2\pi\sigma}} \exp\left[-\frac{(x-t)^2}{2\sigma^2}\right] dt$$

$$= \int_{-\infty}^{\frac{L}{2}} \frac{A}{\sqrt{2\pi\sigma}} \exp\left[-\frac{(t-x)^2}{2\sigma}\right] dt - \int_{-\infty}^{-\frac{L}{2}} \frac{A}{\sqrt{2\pi\sigma}} \exp\left[-\frac{(t-x)^2}{2\sigma}\right] dt$$

$$= A \cdot \left[\Phi\left(\frac{\frac{L}{2}-x}{\sigma}\right) - \Phi\left(\frac{-\frac{L}{2}-x}{\sigma}\right)\right]$$

$$= \frac{\mathrm{A}}{2} \cdot \left[erf\left(\frac{\frac{L}{2}-x}{\sqrt{2}\sigma}\right) - erf\left(\frac{-\frac{L}{2}-x}{\sqrt{2}\sigma}\right)\right] = \frac{\mathrm{A}}{2} \cdot \left[erf\left(\frac{\frac{L}{2}-(x-x_0)}{\sqrt{2}}\right) - erf\left(\frac{-\frac{L}{2}-(x-x_0)}{\sqrt{2}}\right)\right].$$

$F(x;\mu,\sigma^2) = \Phi\left(\frac{x-\mu}{\sigma}\right) = \frac{1}{2}\left[1 + erf\left(\frac{x-\mu}{\sigma\sqrt{2}}\right)\right]$ is the cumulative distribution function (CDF) of $g(x)$, and

$$F(x;0,1) = \Phi(x) = \frac{1}{2}\left[1 + erf\left(\frac{x}{\sqrt{2}}\right)\right].$$

References

[1] M. Bass and V. N. Mahajan, "Handbook of optics. Volume I, Geometrical and physical optics, polarized light, components and instruments," McGraw-Hill, New York.

[2] M. Cutler, "Transillumination of the Breast," *Ann Surg* 93(1), 223-234 (1931)

[3] "Advances in optical imaging and photon migration, Vol. 2 of Topics in Optics and Photonics Series," R. R. Alfano and J. G. Fujimoto, Eds., Optical Society of America, Washington, DC (1996).

[4] W. F. Cheong, S. A. Prahl and A. J. Welch, "A Review of the Optical-Properties of Biological Tissues," *Ieee Journal of Quantum Electronics* 26(12), 2166-2185 (1990)

[5] V. G. Peters, D. R. Wyman, M. S. Patterson and G. L. Frank, "Optical-Properties of Normal and Diseased Human Breast Tissues in the Visible and near-Infrared," *Physics in Medicine and Biology* 35(9), 1317-1334 (1990)

[6] T. L. Troy, D. L. Page and E. M. Sevick-Muraca, "Optical properties of normal and diseased breast tissues: prognosis for optical mammography," *Journal of Biomedical Optics* 1(3), 342-355 (1996)

[7] S. L. Jacques and S. A. Prahl, "ECE532 Biomedical Optics," (1998).

[8] F. F. Jobsis, "Noninvasive, Infrared Monitoring of Cerebral and Myocardial Oxygen Sufficiency and Circulatory Parameters," *Science* 198(4323), 1264-1267 (1977)

[9] J. R. Mourant, A. H. Hielscher, A. A. Eick, T. M. Johnson and J. P. Freyer, "Evidence of intrinsic differences in the light scattering properties of tumorigenic and nontumorigenic cells," *Cancer Cytopathology* 84(6), 366-374 (1998)

[10] A. Santinelli, M. Baccarini, P. Colanzi and G. Fabris, "Microvessel quantitation in intraductal and early invasive breast carcinomas," *Analytical and Quantitative Cytology and Histology* 22(4), 277-284 (2000)

[11] J. C. Hebden and D. T. Delpy, "Enhanced Time-Resolved Imaging with a Diffusion-Model of Photon Transport," *Optics Letters* 19(5), 311-313 (1994)

[12] B. B. Das, K. M. Yoo and R. R. Alfano, "Ultrafast Time-Gated Imaging in Thick Tissues - a Step toward Optical Mammography," *Optics Letters* 18(13), 1092-1094 (1993)

[13] S. Marengo, C. Pepin, T. Goulet and D. Houde, "Time-gated transillumination of objects in highly scattering media using a subpicosecond optical amplifier," *IEEE J. Sel. Top. Quantum Electron.* 5(4), 895-901 (1999)

[14] A. F. Fercher, W. Drexler, C. K. Hitzenberger and T. Lasser, "Optical coherence tomography - principles and applications," *Reports on Progress in Physics* 66(2), 239-303 (2003)

[15] D. Huang, E. A. Swanson, C. P. Lin, J. S. Schuman, W. G. Stinson, W. Chang, M. R. Hee, T. Flotte, K. Gregory, C. A. Puliafito and J. G. Fujimoto, "Optical Coherence Tomography," *Science* 254(5035), 1178-1181 (1991)

[16] M. A. O'Leary, D. A. Boas, B. Chance and A. G. Yodh, "Experimental Images of Heterogeneous Turbid Media by Frequency-Domain Diffusing-Photon Tomography," *Optics Letters* 20(5), 426-428 (1995)

[17] S. B. Colak, D. G. Papaioannou, G. W. 't Hooft, M. B. van der Mark, H. Schomberg, J. C. J. Paasschens, J. B. M. Melissen and N. van Asten, "Tomographic image reconstruction from optical projections in light-diffusing media," *Applied Optics* 36(1), 180-213 (1997)

[18] A. A. Oraevsky, S. L. Jacques and F. K. Tittel, "Measurement of tissue optical properties by time-resolved detection of laser-induced transient stress," *Applied Optics* 36(1), 402-415 (1997)

[19] X. D. Wang, Y. J. Pang, G. Ku, X. Y. Xie, G. Stoica and L. H. V. Wang, "Noninvasive laser-induced photoacoustic tomography for structural and functional in vivo imaging of the brain," *Nature Biotechnology* 21(7), 803-806 (2003)

[20] H. F. Zhang, K. Maslov, G. Stoica and L. H. V. Wang, "Functional photoacoustic microscopy for high-resolution and noninvasive in vivo imaging," *Nature Biotechnology* 24(7), 848-851 (2006)

[21] L. V. Wang and Q. M. Shen, "Sonoluminescent tomography of strongly scattering media," *Optics Letters* 23(7), 561-563 (1998)

[22] L. H. Wang and X. M. Zhao, "Ultrasound-modulated optical tomography of absorbing objects buried in dense tissue-simulating turbid media," *Applied Optics* 36(28), 7277-7282 (1997)

[23] S. Leveque-Fort, "Three-dimensional acousto-optic imaging in biological tissues with parallel signal processing," *Applied Optics* 40(7), 1029-1036 (2001)

[24] M. Kempe, M. Larionov, D. Zaslavsky and A. Z. Genack, "Acousto-optic tomography with multiply scattered light," *Journal of the Optical Society of America a-Optics Image Science and Vision* 14(5), 1151-1158 (1997)

[25] L. H. V. Wang, "Mechanisms of ultrasonic modulation of multiply scattered coherent light: An analytic model," *Phys. Rev. Lett.* 87(4), (2001)

[26] F. J. Blonigen, A. Nieva, C. A. DiMarzio, S. Manneville, L. Sui, G. Maguluri, T. W. Murray and R. A. Roy, "Computations of the acoustically induced phase shifts of optical paths in acoustophotonic imaging with photorefractive-based detection," *Appl. Opt.* 44(18), 3735-3746 (2005)

[27] J. W. Goodman, "Some Fundamental Properties of Speckle," *Journal of the Optical Society of America* 66(11), 1145-1150 (1976)

[28] N. V. Kukhtarev, V. B. Markov, S. G. Odulov, M. S. Soskin and V. L. Vinetskii, "Holographic Storage in Electrooptic Crystals .1. Steady-State," *Ferroelectrics* 22(3-4), 949-960 (1979)

[29] N. V. Kukhtarev, V. B. Markov, S. G. Odulov, M. S. Soskin and V. L. Vinetskii, "Holographic Storage in Electrooptic Crystals .2. Beam Coupling - Light Amplification," *Ferroelectrics* 22(3-4), 961-964 (1979)

[30] L. V. Wang and H.-i. Wu, Biomedical optics : principles and imaging, Wiley-Interscience, Hoboken, N.J. (2007).

[31] H. Liu, B. Beauvoit, M. Kimura and B. Chance, "Dependence of tissue optical properties on solute-induced changes in refractive index and osmolarity," *Journal of Biomedical Optics* 1(2), 200-211 (1996)

[32] V. V. Tuchin, "A clear vision for laser diagnostics (review)," *IEEE J. Sel. Top. Quantum Electron.* 13(6), 1621-1628 (2007)

[33] Z. Yaqoob, D. Psaltis, M. S. Feld and C. H. Yang, "Optical phase conjugation for turbidity suppression in biological samples," *Nature Photonics* 2(2), 110-115 (2008)

[34] I. M. Vellekoop, E. G. van Putten, A. Lagendijk and A. P. Mosk, "Demixing light paths inside disordered metamaterials," *Optics Express* 16(1), 67-80 (2008)

[35] I. M. Vellekoop and A. P. Mosk, "Focusing coherent light through opaque strongly scattering media," *Optics Letters* 32(16), 2309-2311 (2007)

[36] F. A. Marks, H. W. Tomlinson and G. W. Brooksby, "Comprehensive approach to breast cancer detection using light: photon localization by ultrasound modulation and tissue characterization by spectral discrimination," in Photon Migration and Imaging in Random Media and Tissues, pp. 500-510, SPIE, Los Angeles, CA, USA (1993).

[37] S. Leveque, A. C. Boccara, M. Lebec and H. Saint-Jalmes, "Ultrasonic tagging of photon paths in scattering media: parallel speckle modulation processing," *Optics Letters* 24(3), 181-183 (1999)

[38] S. Sakadzic and L. H. V. Wang, "High-resolution ultrasound-modulated optical tomography in biological tissues," *Optics Letters* 29(23), 2770-2772 (2004)

[39] T. W. Murray, L. Sui, G. Maguluri, R. A. Roy, A. Nieva, F. Blonigen and C. A. DiMarzio, "Detection of ultrasound-modulated photons in diffuse media using the photorefractive effect," *Optics Letters* 29(21), 2509-2511 (2004)

[40] W. Leutz and G. Maret, "Ultrasonic Modulation of Multiply Scattered-Light," *Physica B* 204(1-4), 14-19 (1995)

[41] Y. Z. Li, P. Hemmer, C. H. Kim, H. L. Zhang and L. H. V. Wang, "Detection of ultrasound-modulated diffuse photons using spectral-hole burning," *Optics Express* 16(19), 14862-14874 (2008)

[42] Y. Z. Li, H. L. Zhang, C. H. Kim, K. H. Wagner, P. Hemmer and L. V. Wang, "Pulsed ultrasound-modulated optical tomography using spectral-hole burning as a narrowband spectral filter," *Applied Physics Letters* 93(1), (2008)

[43] S. Sakadzic and L. H. V. Wang, "Ultrasonic modulation of multiply scattered coherent light: An analytical model for anisotropically scattering media," *Physical Review E* 66(2), (2002)

[44] A. E. Siegman, "Antenna Properties of Optical Heterodyne Receivers," *Applied Optics* 5(10), 1588-& (1966)

[45] L. Solymar, D. J. Webb and A. Grunnet-Jepsen, The physics and applications of photorefractive materials, Clarendon Press ; Oxford University Press, Oxford [England]; New York (1996).

[46] P. Gunter and J. P. Huignard, Photorefractive materials and their applications 1 basic effects, Springer, New York, NY (2005).

[47] P. Gunter, "Holography, Coherent-Light Amplification and Optical-Phase Conjugation with Photorefractive Materials," *Physics Reports-Review Section of Physics Letters* 93(4), 199-299 (1982)

[48] T. J. Hall, R. Jaura, L. M. Connors and P. D. Foote, "The Photorefractive Effect - a Review," *Progress in Quantum Electronics* 10(2), 77-146 (1985)

[49] S. I. Stepanov, "Applications of Photorefractive Crystals," *Reports on Progress in Physics* 57(1), 39-116 (1994)

[50] L. Sui, T. Murray, G. Maguluri, A. Nieva, F. Blonigen, C. DiMarzio and R. A. Roy, "Enhanced detection of acousto-photonic scattering using a photorefractive crystal," *Proc. SPIE - Int. Soc. Opt. Eng.* 5320(1), 164-171 (2004)

[51] F. Ramaz, B. C. Forget, M. Atlan, A. C. Boccara, M. Gross, P. Delaye and G. Roosen, "Photorefractive detection of tagged photons in ultrasound modulated optical tomography of thick biological tissues," *Optics Express* 12(22), 5469-5474 (2004)

[52] E. Bossy, L. Sui, T. W. Murray and R. A. Roy, "Fusion of conventional ultrasound imaging and acousto-optic sensing by use of a standard pulsed-ultrasound scanner," *Optics Letters* 30(7), 744-746 (2005)

[53] M. Gross, F. Ramaz, B. C. Forget, M. Atlan, C. Boccara, P. Delaye and G. Roosen, "Theoretical description of the photorefractive detection of the ultrasound modulated photons in scattering media," *Optics Express* 13(18), 7097-7112 (2005)

[54] J. Frejlich, Photorefractive materials : fundamental concepts, holographic recording and materials characterization, Wiley-Interscience, Hoboken, N.J. (2007).

[55] M. Bass, G. Li and E. W. Van Stryland, "Handbook of optics. Volume IV, Optical properties of materials, nonlinear optics, quantum optics," McGraw-Hill, New York.

[56] M. W. Roberts, "The photorefractive effect in BSO," San Diego State University (1987).

[57] A. I. o. U. i. Medicine, "Mammalian in vivo ultrasonic biological effects," (1992).

[58] G. Yao and L. H. V. Wang, "Signal dependence and noise source in ultrasound-modulated optical tomography," *Applied Optics* 43(6), 1320-1326 (2004)

[59] K. R. Nightingale, R. W. Nightingale, M. L. Palmeri and G. E. Trahey, "A finite element model of remote palpation of breast lesions using radiation force: Factors affecting tissue displacement," *Ultrasonic Imaging* 22(1), 35-54 (2000)

[60] T. W. Mossberg, "Time-Domain Frequency-Selective Optical-Data Storage," *Optics Letters* 7(2), 77-79 (1982)

[61] L. Menager, I. Lorgere, J. L. Le Gouet, D. Dolfi and J. P. Huignard, "Demonstration of a radio-frequency spectrum analyzer based on spectral hole burning," *Optics Letters* 26(16), 1245-1247 (2001)

[62] Y. Z. Li, A. Hoskins, F. Schlottau, K. H. Wagner, C. Embry and W. R. Babbitt, "Ultrawideband coherent noise lidar range-Doppler imaging and signal processing by use of spatial-spectral holography in inhomogeneously broadened absorbers," *Applied Optics* 45(25), 6409-6420 (2006)

[63] L. Allen and J. H. Eberly, Optical resonance and two-level atoms, Wiley, New York (1975).

[64] M. Mitsunaga and R. G. Brewer, "Generalized Perturbation-Theory of Coherent Optical-Emission," *Physical Review A* 32(3), 1605-1613 (1985)

[65] M. Colice, F. Schlottau and K. H. Wagner, "Broadband radio-frequency spectrum analysis in spectral-hole-burning media," *Applied Optics* 45(25), 6393-6408 (2006)

[66] G. Gorju, V. Crozatier, I. Lorgere, J. L. Le Gouet and F. Bretenaker, "10-GHz bandwidth RF spectral analyzer with MHz resolution based on spectral hole burning in Tm3+ : YAG," *Ieee Photonics Technology Letters* 17(11), 2385-2387 (2005)

[67] S. R. Kothapalli, S. Sakadzic, C. Kim and L. V. Wang, "Imaging optically scattering objects with ultrasound-modulated optical tomography," *Optics Letters* 32(16), 2351-2353 (2007)

[68] K. Sri-Rajasekhar, S. Sava, K. Chulhong and V. W. Lihong, "Imaging of optical scattering contrast using ultrasound-modulated optical tomography," A. O. Alexander and V. W. Lihong, Eds., p. 68561P, SPIE (2008).

[69] H. Zhang, M. Sabooni, L. Rippe, S. Kroll, C. Kim, L. H. Wang and P. Hemmer, "Deep tissue (phantom) imaging with spectral hole burning in Pr:YSO," (2011)

[70] C. A. Primmerman, D. V. Murphy, D. A. Page, B. G. Zollars and H. T. Barclay, "Compensation of Atmospheric Optical Distortion Using a Synthetic Beacon," *Nature* 353(6340), 141-143 (1991)

[71] S. M. Popoff, G. Lerosey, R. Carminati, M. Fink, A. C. Boccara and S. Gigan, "Measuring the Transmission Matrix in Optics: An Approach to the Study and Control of Light Propagation in Disordered Media," *Phys. Rev. Lett.* 104(10), 100601-100604 (2010)

[72] I. M. Vellekoop, A. Lagendijk and A. P. Mosk, "Exploiting disorder for perfect focusing," *Nature Photonics* 4(5), 320-322 (2010)

[73] A. Ishimaru, Wave propagation and scattering in random media, Academic Press, New York (1978).

[74] M. Fink, D. Cassereau, A. Derode, C. Prada, P. Roux, M. Tanter, J. L. Thomas and F. Wu, "Time-reversed acoustics," *Reports on Progress in Physics* 63(12), 1933-1995 (2000)

[75] G. Lerosey, J. De Rosny, A. Tourin and M. Fink, "Focusing beyond the diffraction limit with far-field time reversal," *Science* 315(5815), 1120-1122 (2007)

[76] G. D. Mahan, W. E. Engler, J. J. Tiemann and E. Uzgiris, "Ultrasonic tagging of light: Theory," *Proc. Natl. Acad. Sci. U. S. A.* 95(24), 14015-14019 (1998)

[77] G. S. He, "Optical phase conjugation: principles, techniques, and applications," *Progress in Quantum Electronics* 26(3), 131-191 (2002)

[78] R. A. Fisher, Optical phase conjugation, Academic Press, New York, N.Y. (1983).

[79] A. Yariv, "Phase Conjugate Optics and Real-Time Holography," *Ieee Journal of Quantum Electronics* 14(9), 650-660 (1978)

[80] X. Xu, H. L. Zhang, P. Hemmer, D. K. Qing, C. Kim and L. V. Wang, "Photorefractive detection of tissue optical and mechanical properties by ultrasound modulated optical tomography," *Optics Letters* 32(6), 656-658 (2007)

[81] L. H. Wang, S. L. Jacques and L. Q. Zheng, "Mcml - Monte-Carlo Modeling of Light Transport in Multilayered Tissues," *Computer Methods and Programs in Biomedicine* 47(2), 131-146 (1995)

[82] S. Srinivasan, B. W. Pogue, S. D. Jiang, H. Dehghani, C. Kogel, S. Soho, J. J. Gibson, T. D. Tosteson, S. P. Poplack and K. D. Paulsen, "Interpreting hemoglobin and water concentration, oxygen saturation, and scattering measured in vivo by near-infrared breast tomography," *Proc. Natl. Acad. Sci. U. S. A.* 100(21), 12349-12354 (2003)

[83] M. Gross, M. Lesaffre, F. Ramaz, P. Delaye, G. Roosen and A. C. Boccara, "Detection of the tagged or untagged photons in acousto-optic imaging of thick highly scattering media by photorefractive adaptive holography," *European Physical Journal E* 28(2), 173-182 (2009)

[84] H. L. Liu, X. Xu, P. Lai and L. H. Wang, "Time-reversed ultrasonically encoded optical focusing into tissue-mimicking media with optical thickness up to 70," *Journal of Biomedical Optics* (2011)

[85] X. Xu, H. L. Liu and L. V. Wang, "Time-reversed ultrasonically encoded optical focusing into scattering media," *Nature Photonics* 5(3), 154-157 (2011)

Vita

Xiao Xu

Date of Birth	September 23, 1972
Place of Birth	Hu Zhou, China
Degrees	Ph.D. Biomedical Engineering, August 2011 M.S. Physics, May 2002 B.S. Physics, July 1995
Professional Societies	SPIE
Publications	Xu, X., Liu, H. & Wang, L. V. Time-reversed ultrasonically encoded optical focusing into scattering media. *Nature Photon.* **5**, 154-157 (2011). Xu, X., Kothapalli, S., Liu, H. & Wang, L. V. Spectral hole burning for ultrasound-modulated optical tomography of thick tissue," *J. Biomed. Opt.* **15**, 066018 (2010). Xu, X. *et al.* Photorefractive detection of tissue optical and mechanical properties by ultrasound modulated optical tomography. *Opt. Lett.* **32**, 656–658 (2007).

August 2011